

Article

Band-Gap Engineering of Layered Perovskites by Cu Spacer Insertion as Photocatalysts for Depollution Reaction

Monica Raciulete ¹, Crina Anastasescu ¹, Florica Papa ^{1,*} , Irina Atkinson ¹ , Corina Bradu ^{2,3} , Catalin Negrila ⁴, Diana-Ioana Eftemie ¹, Daniela C. Culita ¹ , Akane Miyazaki ⁵, Veronica Bratan ¹, Jeanina Pandeale-Cusu ¹, Cornel Munteanu ¹, Gianina Dobrescu ¹, Alexandra Sandulescu ¹ and Ioan Balint ^{1,*}

¹ “Ilie Murgulescu” Institute of Physical Chemistry of the Romanian Academy, 202 Spl. Independentei, 060021 Bucharest, Romania

² PROTMed Research Center, University of Bucharest, 91–95 Spl. Independentei, 050107 Bucharest, Romania

³ Faculty of Biology, University of Bucharest, 91–95 Spl. Independentei, 050095 Bucharest, Romania

⁴ National Institute of Material Physics, 077125 Magurele, Romania

⁵ Department of Chemical and Biological Sciences, Faculty of Science, Japan Women’s University, 2-8-1 Mejirodai, Bunkyo-ku, Tokyo 112-8681, Japan

* Correspondence: frusu@icf.ro (F.P.); ibalint@icf.ro (I.B.)

Abstract: A multi-step ion-exchange methodology was developed for the fabrication of Cu(LaTa₂O₇)₂ lamellar architectures capable of wastewater depollution. The (001) diffraction line of RbLaTa₂O₇ depended on the guest species hosted by the starting material. SEM and TEM images confirmed the well-preserved lamellar structure for all intercalated layered perovskites. The UV–Vis, XPS, and photocurrent spectroscopies proved that Cu intercalation induces a red-shift band gap compared to the perovskite host. Moreover, the UV–Vis spectroscopy elucidated the copper ions environment in the Cu-modified layered perovskites. H₂-TPR results confirmed that Cu species located on the surface are reduced at a lower temperature while those from the interlayer occur at higher temperature ranges. The photocatalytic degradation of phenol under simulated solar irradiation was used as a model reaction to assess the performances of the studied catalysts. Increased photocatalytic activity was observed for Cu-modified layered perovskites compared to RbLaTa₂O₇ pristine. This behavior resulted from the efficient separation of photogenerated charge carriers and light absorption induced by copper spacer insertion.

Keywords: copper spacer; layered perovskite; phenol; photocatalysis; simulated solar irradiation



Citation: Raciulete, M.; Anastasescu, C.; Papa, F.; Atkinson, I.; Bradu, C.; Negrila, C.; Eftemie, D.-I.; Culita, D.C.; Miyazaki, A.; Bratan, V.; et al. Band-Gap Engineering of Layered Perovskites by Cu Spacer Insertion as Photocatalysts for Depollution Reaction. *Catalysts* **2022**, *12*, 1529. <https://doi.org/10.3390/catal12121529>

Academic Editor: Leonarda Liotta

Received: 18 October 2022

Accepted: 22 November 2022

Published: 27 November 2022

Publisher’s Note: MDPI stays neutral with regard to jurisdictional claims in published maps and institutional affiliations.



Copyright: © 2022 by the authors. Licensee MDPI, Basel, Switzerland. This article is an open access article distributed under the terms and conditions of the Creative Commons Attribution (CC BY) license (<https://creativecommons.org/licenses/by/4.0/>).

1. Introduction

Layered perovskites represent an emerging class of materials whose applications are constantly rising in various fields spanning from dielectrics [1], superconductivity [2], or luminescence [3] to catalysis and photocatalysis [4,5]. The development of stable, low-cost, and high-efficiency photocatalysts that utilize solar energy could solve many environmental concerns [6]. Among various semiconductors, Dion-Jacobson (DJ)-type layered perovskites are effective photocatalysts for water splitting under solar light irradiation [7]. Their interlamellar space allows for achieving stronger light absorption with more efficient charge carrier separation. In this way, the photocatalytic performance of the new composites dramatically increases.

The class of DJ perovskites possesses a composition of M[A_{n−1}B_nO_{3n+1}], where M is an alkali metal, A is a lanthanide, B is a d⁰ transitional metal, and n is the number of BO₆ octahedra. For example, the 2D blocks of RbLaTa₂O₇ are composed of corner-shared TaO₆ octahedra, interleaved with 12 coordinate La³⁺ cations, and separated by a Rb⁺ interlayer cation. An essential feature of these materials consists of their ability to accommodate a variety of spacers into the inorganic matrix while the structure of

perovskite blocks remains unchanged. Due to the layered structure flexibility, their physico-chemical properties are tailored through ion exchange, pillaring, exfoliation, or restacking methods [8]. Compounds such as clay minerals, graphite, and transition metal dichalcogenides are known to accommodate guest species in their interlayer space. Therefore, a unique nanoarchitecture with attractive properties is obtained compared to those of the parental materials. Layered perovskites are amenable to alkali-proton exchange reactions to obtain solid acid phases. Protons located between galleries can be further exchanged with various molecules (alcohols, amines, phosphorous, alcohols, and carboxylic acids) leading to new organic-inorganic hybrid compounds [9,10]. Exfoliation into ultrathin nanosheets is feasible for the fabrication of nanostructured devices [11] or used as building blocks for novel materials [12]. It is worth noting that the size and configuration of the spacer cation influence the physicochemical properties of the photocatalysts [13]. The recent work by Minich et al. [14] revealed that the interlayer water plays a crucial role in the formation of *n*-alkylamines intercalated perovskite-like bismuth titanate $\text{H}_2\text{K}_{0.5}\text{Bi}_{2.5}\text{Ti}_4\text{O}_{13} \cdot \text{H}_2\text{O}$. Fan et al. [15] demonstrated that (Pt, TiO_2) intercalated HLaNb_2O_7 possesses superior photocatalytic H_2 evolution compared to unmodified TiO_2 . Wu and coworkers [16] fabricated $\text{Fe}_2\text{O}_3/\text{HLaNb}_2\text{O}_7$ through an intercalation route, which showed an enhanced hydrogen production rate compared to individual oxides.

An approach to improve the charge separation efficiency in layered perovskites refers to noble metal intercalation at specific interlayer sites. As an example, RuO_2 - [17] and Pt- [18] intercalated $\text{KCa}_2\text{Nb}_3\text{O}_{10}$ possess high photocatalytic performance for water splitting. Unfortunately, the high cost, the limited availability, as well as the non-uniform distribution of these guests restrict their practical application. Regarding the photocatalysis field, TiO_2 has served as a benchmark of light-related photocatalytic processes. However, its large band gap, the fast carrier recombination, or the particle agglomerations are factors that limit the TiO_2 efficiency. To overcome these drawbacks, searching for innovative functional materials for (i) expanding the light-harvesting wavelength range and (ii) suppressing the quick recombination of photogenerated charge carriers is highly desirable.

Copper oxide p-type semiconductors have become a promising alternative in the field of catalysis, photovoltaics, and energy storage applications [19]. These materials possess outstanding properties, such as narrow band gap, non-toxicity, and low price. CuO has a band gap of 1.21–2.1 eV and a monoclinic crystal structure, while Cu_2O has a band gap of 2.2–2.9 eV and a cubic crystal structure [20]. Alternatively, the interlayer gallery of the layered perovskites provides a space-confined environment for the exchangeable ions.

One strategy for developing visible-light-driven photocatalysts is to create a new valence band (VB) located at more negative potentials than O 2p orbitals, giving rise to a narrower band gap [21]. Recently, new visible-light-driven H_2 - and O_2 - evolving photocatalysts have been developed by Ag^+ and Cu^+ alkali-ion exchanges in various wide-band-gap perovskites [22]. Similarly, Cu(I)-ion-exchanged $\text{K}_2\text{La}_2\text{Ti}_3\text{O}_{10}$ photocatalysts demonstrated enhanced activity for H_2 production with a response up to 620 nm [23]. Therefore, engineering the interlayer spacing of lamellar materials is a reliable route to improve photocatalytic performance.

Phenolic compounds are a class of ubiquitous contaminants frequently present in wastewater due to their employment in industry and human activities [24]. Alternative approaches have been developed over the last few decades to remove persistent organic pollutants [25]. The photocatalytic mineralization process remains one of the most attractive technologies for the degradation of recalcitrant contaminants contained in water sources into harmless CO_2 and H_2O . Its efficiency is due to reactive oxygen species generated by the photocatalyst during light exposure that degrade the hazardous compounds.

We report a versatile route to fabricate a novel $\text{Cu}(\text{LaTa}_2\text{O}_7)_2$ layered architecture through the modification of the $\text{RbLaTa}_2\text{O}_7$ host via protonation-amine intercalation steps. One aim of this work was to explore the nature and role of copper species (interlayer and/or surface) on the physico-chemical properties of the $\text{Cu}(\text{LaTa}_2\text{O}_7)_2$ matrix. The ultimate goal

was to study the photocatalytic degradation of phenol under simulated solar irradiation over the new $\text{Cu}(\text{LaTa}_2\text{O}_7)_2$ assemblies, depending on their thermal treatments.

2. Results and Discussion

2.1. Crystal Structure and Morphology

The XRD patterns for the pristine layered perovskite (RbLTO), proton-exchanged form (HLTO), *n*-butylamine-derived perovskite (BuALTO), copper-intercalated perovskite (CuLTO), copper-intercalated perovskite calcined at 500 °C (CuLTO-500C), and copper-intercalated perovskite reduced at 800 °C (CuLTO-800R) were collected in Figure 1. The lattice parameters and the phase composition of the synthesized materials are listed in Table 1.

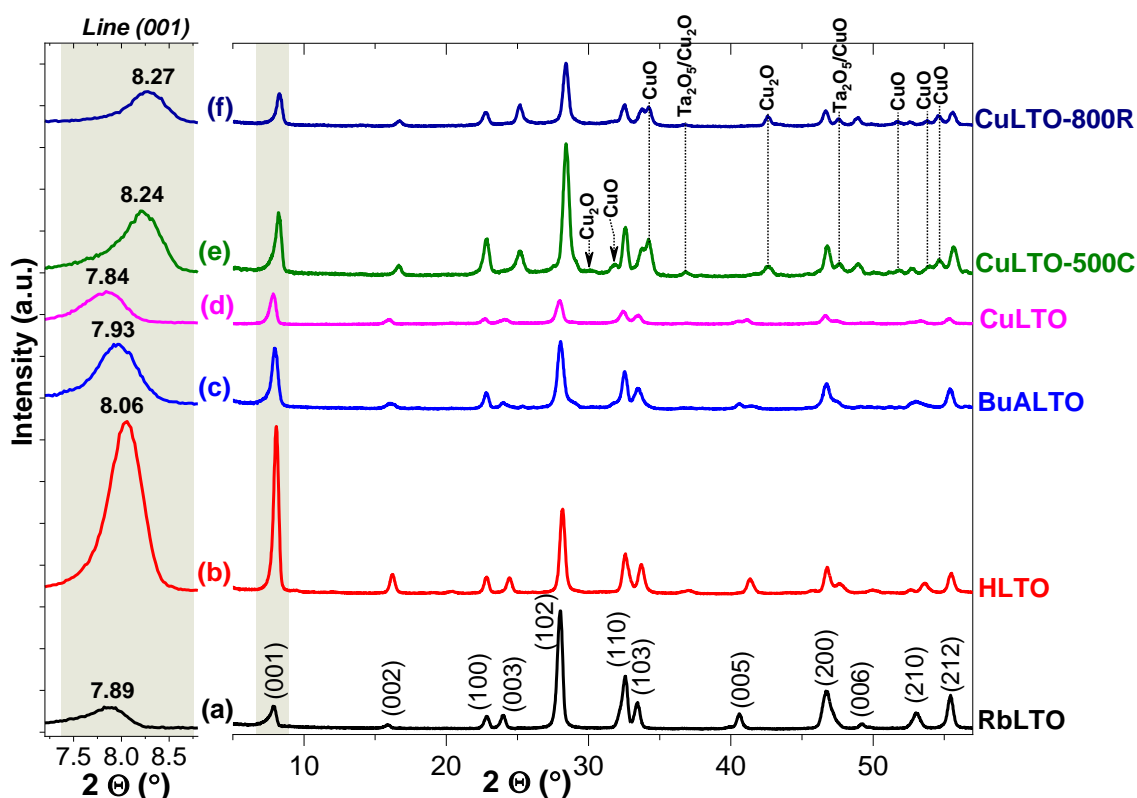


Figure 1. XRD patterns of (a) RbLTO, (b) HLTO, (c) BuALTO, (d) CuLTO, (e) CuLTO-500C, (f) CuLTO-800R. In brackets are given the Miller indices of the $\text{RbLaTa}_2\text{O}_7$ phase.

Table 1. Lattice parameters, *d*-spacing, gallery height, and phase composition for the RbLTO host and its guest-intercalated products.

Sample	Lattice Parameters		<i>d</i> -Spacing for $l_{(001)}$, (Å)	Gallery Height (Å)	Phase Composition
	<i>a</i> (Å)	<i>c</i> (Å)			
RbLTO	3.881	11.121	11.185	3.69	RbLaTa ₂ O ₇
HLTO	3.883	10.924	10.951	3.45	HLTa ₂ O ₇
BuALTO	3.889	11.113	11.113	3.61	(C ₄ H ₁₁ N)LaTa ₂ O ₇
CuLTO	3.888	11.023	11.228	3.73	Cu(LaTa ₂ O ₇) ₂
CuLTO-500C	3.880	10.718	10.719	3.22	Cu(LaTa ₂ O ₇) ₂ , Cu ₂ O, CuO, Ta ₂ O ₅
CuLTO-800R	3.884	10.676	10.676	3.18	Cu(LaTa ₂ O ₇) ₂ , Cu ₂ O, CuO, Ta ₂ O ₅

The XRD pattern of the RbLTO solid shows the $\text{RbLaTa}_2\text{O}_7$ structure with tetragonal symmetry ($P4/mmm$, cell parameters $a = 3.881$ and $c = 11.121$ Å, PDF card no. 01-089-0389). Acid treatment of pristine produced the HLaTa_2O_7 phase (PDF card no. 01-081-1194), in accordance with previously reported data for proton-exchanged compounds. The protonation step left the a parameter unchanged, while the (001) diffraction line was shifted towards higher 2Θ angles (8.06°). This fact indicates a smaller c parameter for the HLTO solid. Subsequent treatment of the proton-exchanged perovskite with n -butylamine ($n\text{-C}_4\text{H}_9\text{-NH}_2$) leads to a shift of the (001) reflection at a lower 2Θ angle (7.93°) in BuALTO solid. This shift is a consequence of the amine's intercalation into the protonated perovskite's interlayer spaces. Onward, the intercalation of the Cu^{2+} spacer into the BuALTO solid resulted in a further shift of the (001) line to lower angles ($2\Theta = 7.84^\circ$). This observation indicates that copper was introduced in between the $[\text{LaTa}_2\text{O}_7]^-$ layers. The benefit of using the n -butylamine as an intercalation precursor is that of forming a complex with the metallic ion. From this standpoint, $[\text{Cu}(\text{NH}_2\text{-C}_4\text{H}_9)_4(\text{H}_2\text{O})_2]^{2+}$ can be considered as a vector to incorporate copper into perovskite layers.

The XRD patterns of both CuLTO-500C and CuLTO-800R reveal the preservation of the stratified structure but also the presence of distinctive lines attributed to Cu_2O (PDF card no. 01-078-2076), CuO (PDF card no. 01-089-5895), and Ta_2O_5 (PDF card no. 00-018-1304) crystalline phases. Figure 2B shows that either the calcination or reducing treatments of CuLTO solid resulted in the dramatic shortening of the d -distance. Thus, values of 10.719 Å for CuLTO-500C and 10.676 Å for CuLTO-800C were observed in comparison to the pristine layered perovskite.

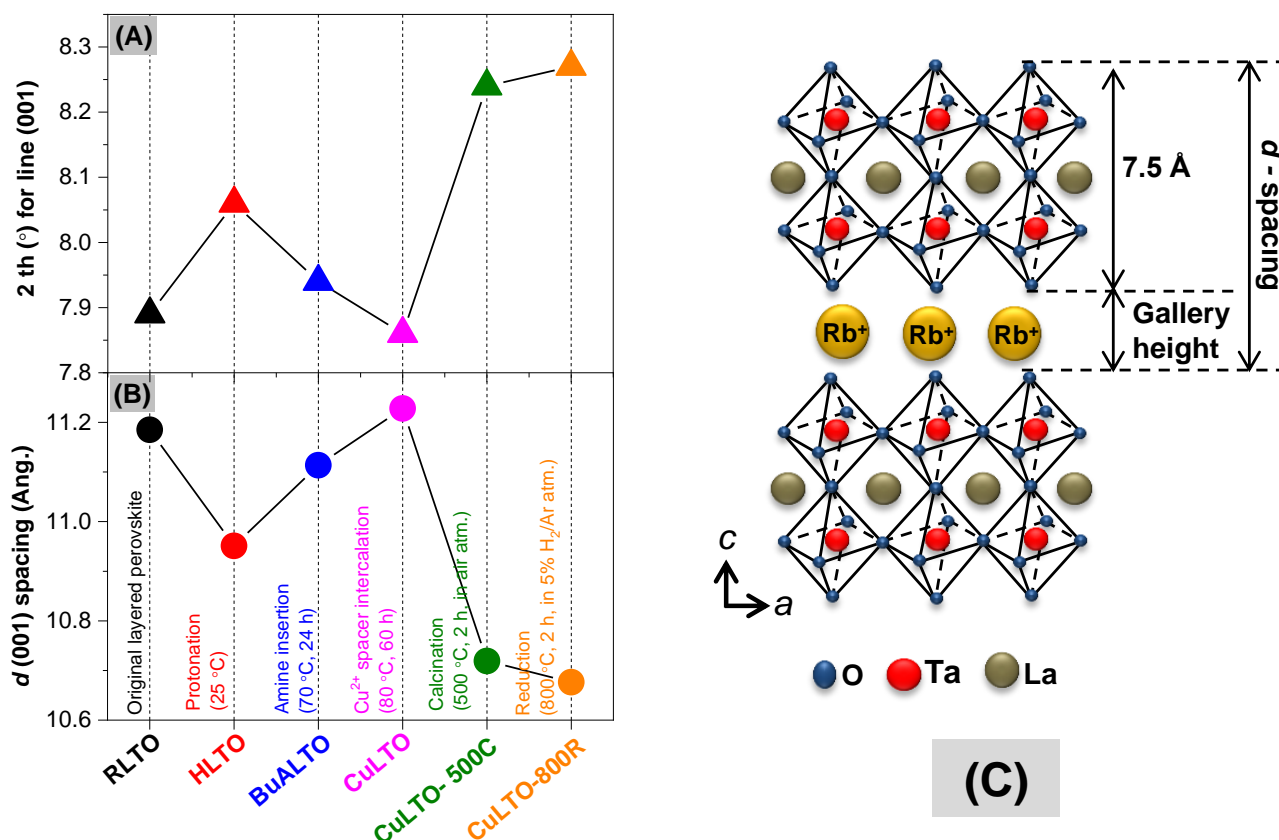


Figure 2. Evolution of the (A) 2-theta and (B) d -spacing of the RbLTO host and its guest-intercalated spacers. The layered perovskite structure of $\text{RbLaTa}_2\text{O}_7$ is schematically given in (C).

The nature of the spacer influences the overall structure of the newly assembled compound as it can distort the perovskite from its ideal structure through the tilting of the

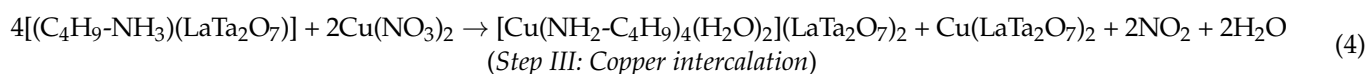
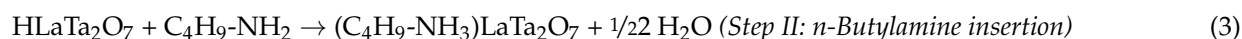
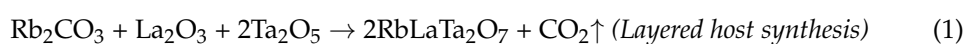
oxygen octahedra, the shifting of the layers, or Jahn-Teller distortions [26]. The shortening of the *c*-axis of the $\text{CuLa}_2\text{Ti}_3\text{O}_{10}$ compound was observed by Hyeon et al. after the solid was heated up to 700 °C [27]. The authors attributed this contraction to the flattening of the CuO_4 unit toward quasi-square planar coordination. Ogawa and Kuroda [28] reported that the alkyl-ammonium ions intercalated layered silicates are aligned parallel to the silicate sheets. Similarly, Sasaki et al. [29] indicated two modes of accommodation of the alkyl chain into the titanate layered structure. For a chain length up to the carbon number of three (C_3), a nearly parallel arrangement has been suggested, while for C_5 or more, the interlayer distance expanded linearly with an increase in the chain length. These authors claimed that in the case of butylamine, both types of arrangement coexisted (flat or perpendicular). In another study regarding layered titanate-intercalated pyridine, two values of the *d*-spacing were reported: (i) a value of 3 Å when pyridine was inserted flat into the interlayer space and (ii) 5.8 Å when pyridine was intercalated perpendicular to the surface [30]. The chain length of the butylamine has a value of 7.6 Å, and its alkyl chain usually tilts or overlaps [31].

Collectively, our results appear to be consistent with the literature review. We suppose that *n*-butylamine was inserted in between the layers of the BuALTO solid in such a way, probably in a flat orientation, that it does not significantly expand the d_{001} spacing.

Figure 2A displays the variation of the *d*-spacing and 2- θ angle for the (001) line diffraction over the synthesized materials attributed to the $\text{RbLaTa}_2\text{O}_7$ host structure (Figure 2B).

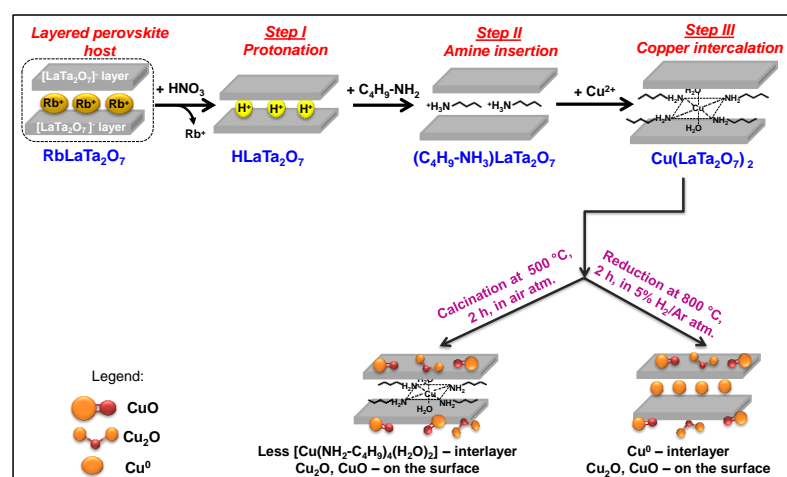
The gallery height was calculated by the difference between the *d* values derived from the (001) reflection peaks of all the solids and the perovskite layer thickness (~7.5 Å) [16]. Table 1 gives the interlayer heights of the RbLTO host and its guest-intercalated spacers. The results underline that the gallery height of the solids is spacer-related.

The chemical reactions that take place after each synthesis step are described in Equations (1)–(4):



The methodology of replacing Rb^+ with Cu^{2+} in the $\text{RbLaTa}_2\text{O}_7$ interlayer host proceeds in three steps (Scheme 1). The first step involves the exchange of the interlayer rubidium cation with H^+ via protonation (step I, Equation (2)). The next stage consists of the expansion of the galleries of proton-exchanged layered perovskite by introducing a spacer such as *n*-butylamine (step II, Equation (3)). The role of the alkylamine is not only to increase the interlayer distance but also to form a [Cu-amine] complex, thus favoring the intercalation of Cu into the perovskite host (step III, Equation (4)).

Thermogravimetric (TG) analyses additionally confirm the various spacers inserted into the $\text{RbLaTa}_2\text{O}_7$ host. The TG curves of the HLTO, BuALTO, CuLTO, CuLTO-500C, and CuLTO-800R materials showed several stages of mass losses as a function of temperature. The obtained results are listed in Table S1 from supporting information. For comparison, the TG curve of RbLTO pristine is also given in Figure 3A, while its description was presented elsewhere [32]. The first peak centered at 134 °C is due to the elimination of adsorbed water, while the second peak at 305 °C corresponds to a partial dehydration of lanthanum oxide. After 600 °C, take place the elimination of CO_2 .



Scheme 1. Schematic pathway of $\text{Cu}(\text{LaTa}_2\text{O}_7)_2$ synthesis followed by the two different thermal treatments.

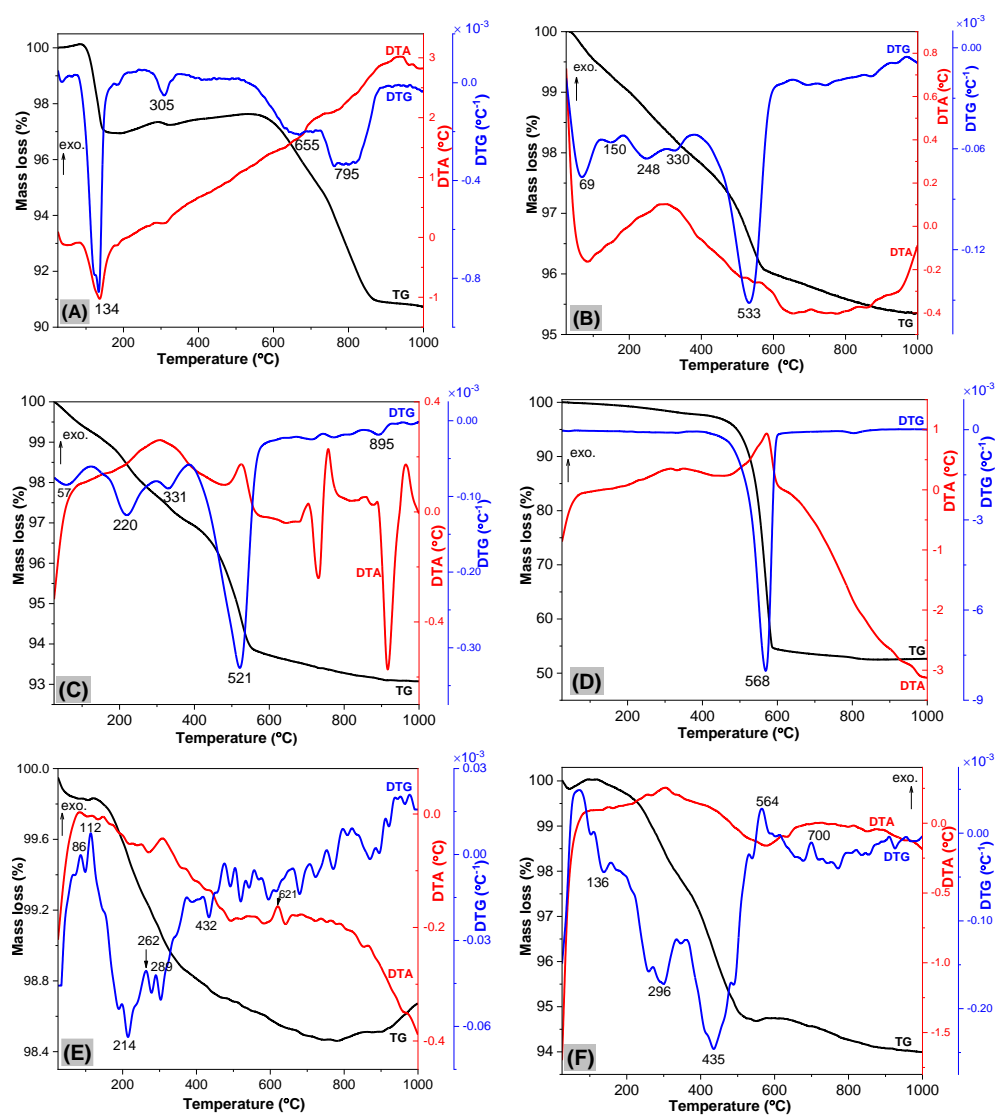
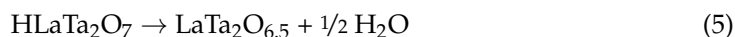


Figure 3. Thermogravimetric curves (TG, DTG, DTA) of (B) HLTO, (C) BuALTO, (D) CuLTO, (E) CuLTO-500C, and (F) CuLTO-800R, measured in an air atmosphere with a heating rate of $10\text{ }^{\circ}\text{C}\cdot\text{min}^{-1}$. The TG curve of the RbLTO host is given for comparison in (A) [32].

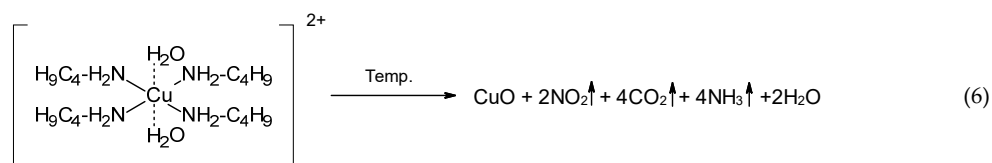
For the HLTO sample, (Figure 3B) water elimination from 25 to 380 °C in four steps is associated with the removal of the adsorbed water. The experimental value of the measured weight loss (2.00%) was close to the theoretical value of 2.93%. The calculated value corresponds to 1 mole H₂O per [LaTa₂O₇][−] unit formula of protonated perovskite. The mass loss of 1.37% (peak at 533 °C) is due to the loss of the interlayer proton as water, according to Equation (5). The last step on the TG curve (650–1000 °C) indicates negligible mass loss (0.32%), showing that the deprotonation process is completed up to 650 °C.



The theoretical weight loss should be 1.48% if all Rb⁺ cations replaced by protons are located in the interlayer space. According to these data, a protonation degree of 93% has been achieved in the HLTO solid. The successful protonation step was also confirmed by ion chromatography showing that 99.2% Rb⁺ cations were replaced by H⁺ during the acid treatment of the RbLaTa₂O₇ host with nitric acid. This result is consistent with reports in the literature for other related protonated layered perovskites.

Thermal analysis attests that *n*-butylamine was intercalated and helps to quantify the amount of the inserted amine. The first mass loss (25–124 °C) of the BuALTO (Figure 3C) is attributed to the elimination of adsorbed water. In the temperature range of 124–1000 °C, the total weight loss of 6.36% is assigned to the elimination of amine, which takes place in multiple steps. In the study of Geselbracht et al. [33], the total mass loss of the hexylamine-intercalated HCa₂Nb_{3−x}Ta_xO₁₀ has been calculated in the domain of 25–900 °C. In the research work on octylamine-intercalated layered vanadium oxide, the authors ascribed the weight loss at low-temperature to the release of free amine molecules, while the higher-temperature one was attributed to the combustion of interlayer amine [34]. For this study, the complete decomposition of the inserted *n*-butylamine takes place in multiple steps. The peak at 521 °C observed on the TG curve of the BuALTO solid certifies that the butylamine is located in the interlayer position. Its experimental mass loss was determined to be 3.61%. The calculated weight loss for the amine total decomposition should be 10.64%, while a lower experimental value was found. It implies that only 33.92% of the butylamine was located in between the [LaTa₂O₇][−] layers.

After the insertion of the Cu²⁺ spacer (Figure 3D), the metal-ligand complex [Cu(NH₂-C₄H₉)₄(H₂O)₂] is formed. The large mass loss of 43.39% observed for CuLTO is indicative of [Cu-amine] complex decomposition with the elimination of gaseous NO₂, CO₂, and NH₃ compounds, Equation (6).



The TG curves of the CuLTO-500C and CuLTO-800R samples (Figure 3E,F) show different behavior compared to the HLTO, BuALTO, and CuLTO layered perovskites. Various exothermic effects observed on the DTA curves of both thermally treated materials could signify a possible phase transition. Indeed, the presence of copper phases on CuLTO-500C and CuLTO-800R was subsequently probed by XRD analysis (Figure 1).

SEM images of RbLTO, HLTO, BuALTO, and Cu-modified layered perovskites are shown in Figure 4A–E. The well-preserved lamellar structure of the starting material is observed for all studied architectures. The synthesized Rb- and H- forms do not show significant particle size differences. On the other hand, the particles of BuA- and Cu-intercalated products tend to form lamellar agglomerates with a smaller size as compared to RbLTO's original layered perovskite. The transmission electron microscopy (TEM) images further confirm that both *n*-butylamine- and Cu-based layered perovskites (Figure 5A–F) retain their stratified structures.

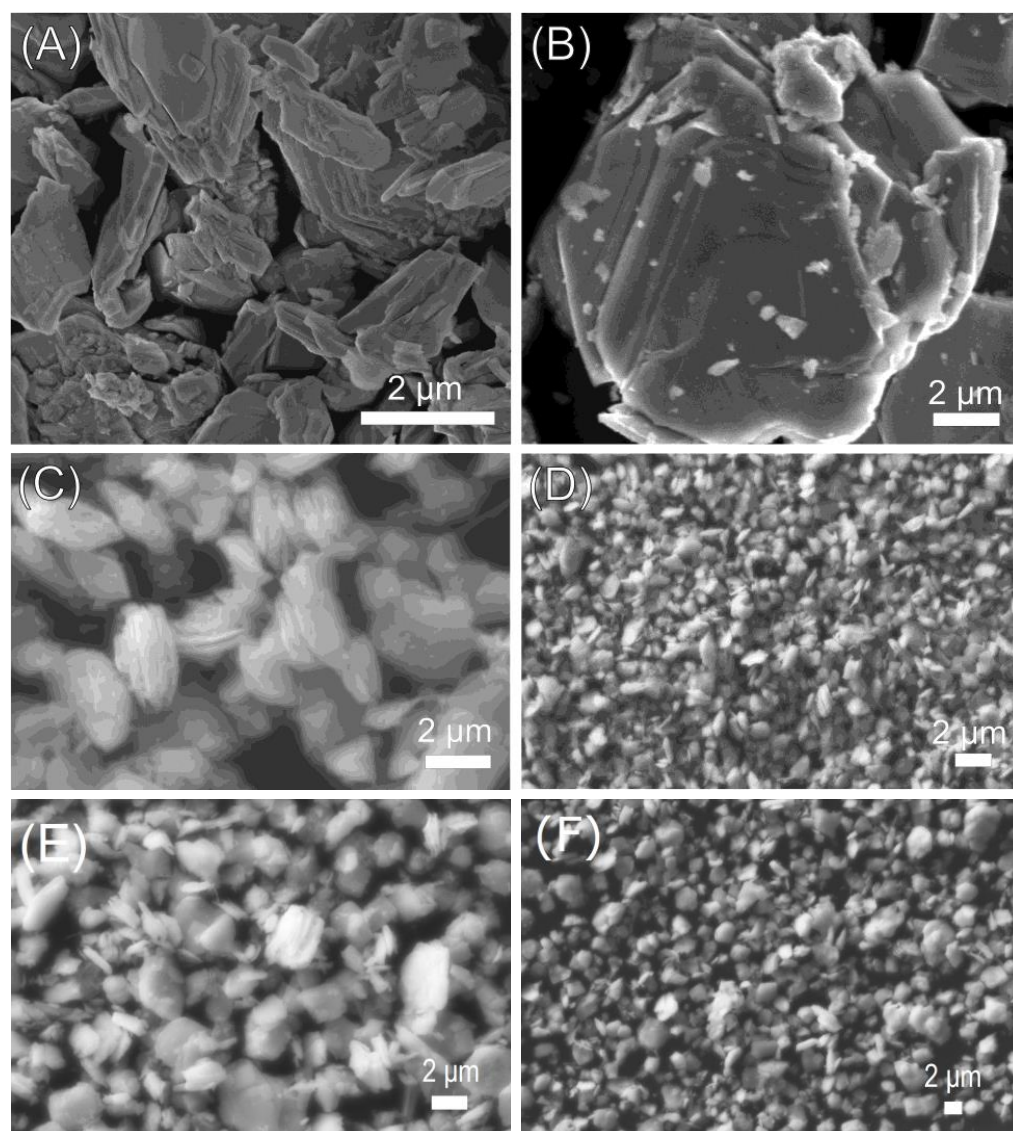


Figure 4. SEM images of (A) RbLTO, (B) HLTO, (C) BuALTO, (D) CuLTO, (E) CuLTO-500C, and (F) CuLTO-800R materials.

The elemental mapping images (Figure 6) show that in the BuALTO and CuLTO compounds, La, Ta, and O are homogeneously distributed within each sample. No presence of rubidium was observed. This observation demonstrated that the cation exchange took place. The presence of a copper peak in the CuLTO novel architecture (Figure 6B) demonstrates the successful Cu intercalation process.

Table 2 reports the surface chemical composition of RbLTO, CuLTO, CuLTO-500C, and CuLTO-800R perovskites as determined by XPS analysis. The results illustrate that the surface composition of the solids changes, depending on the applied thermal treatment (as fresh, calcination, and reduction). Notably, the bulk of the Cu-modified perovskites is constantly preserved as a $\text{Cu}(\text{LaTa}_2\text{O}_7)_2$ crystalline phase. This observation is confirmed by the XRD patterns (Figure 1).

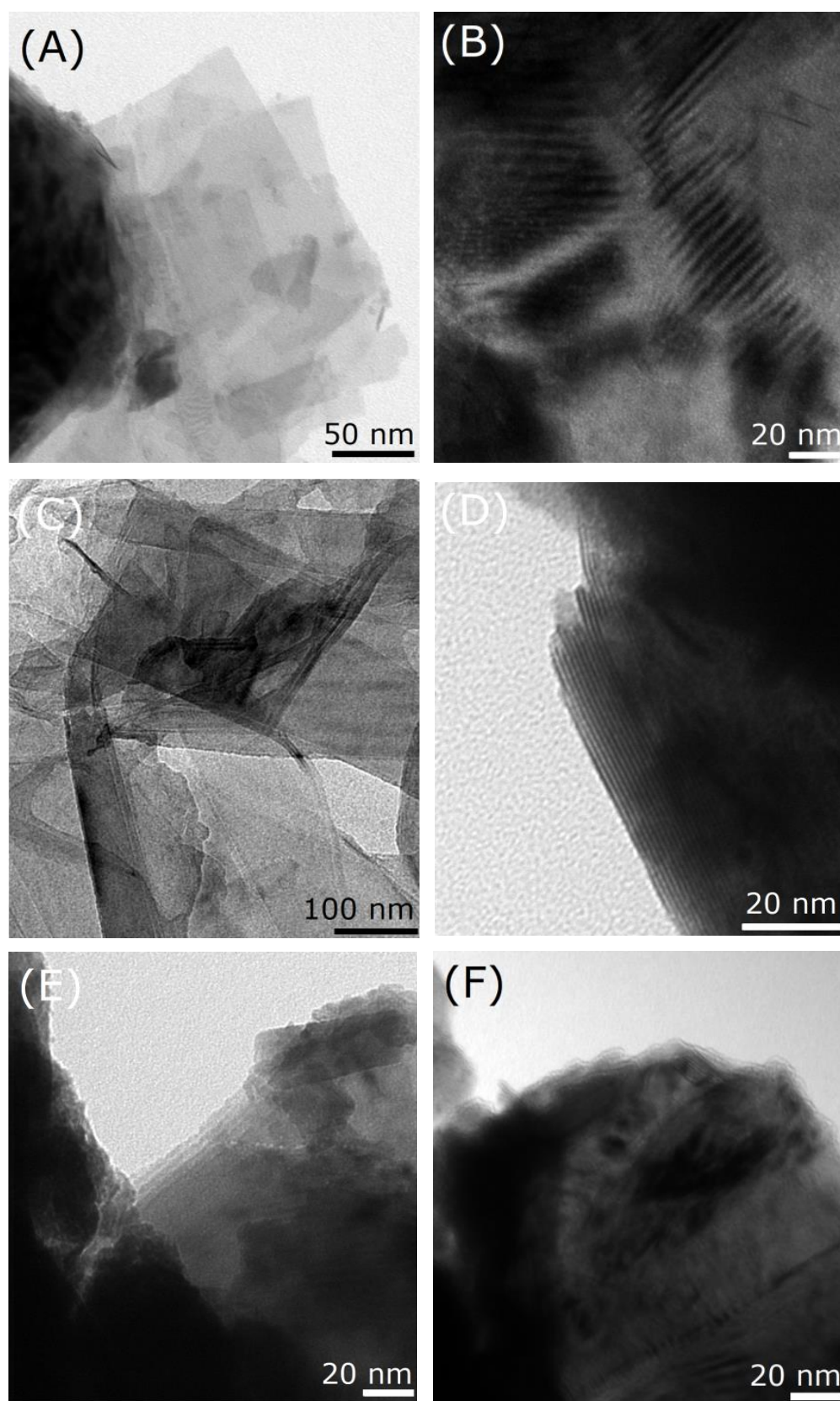


Figure 5. TEM images of (A,B) BuALTO, (C,D) CuLTO, (E) CuLTO-500C, and (F) CuLTO-800R.

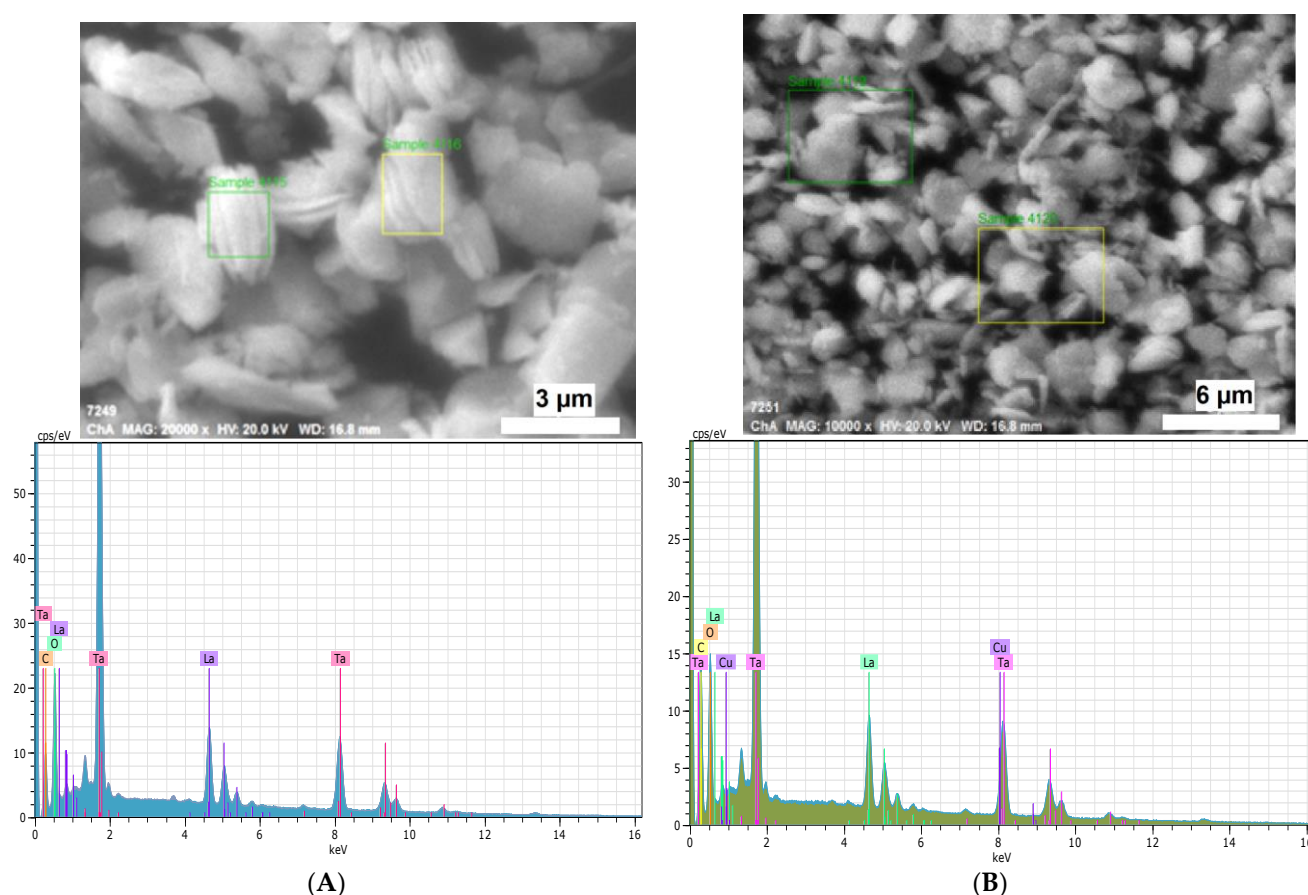


Figure 6. SEM-EDS elemental mapping images of (A) BuALTO and (B) CuLTO lamellar structures for O, La, Ta, and Cu elements.

Table 2. Surface chemical composition and atomic ratio determined by XPS analysis for RbLTO host and its guest-intercalated products.

Sample	Chemical Analysis of the Products (at. %)						Atomic Ratio
	Rb (%)	C (%)	O (%)	La (%)	Ta (%)	Cu (%)	Cu/(La + Ta)
RbLTO	10.0	39.6	36.5	5.4	8.5	0.0	0.00
CuLTO	0.0	67.0	32.9	0.0	0.0	0.1	0.00
CuLTO-500C	0.0	33.3	58.4	1.5	5.6	1.3	0.18
CuLTO-800R	0.0	39.3	45.1	3.1	8.9	3.5	0.29

The Cu/(La + Ta) surface atomic ratio of Cu-intercalated layered perovskites is slightly decreased compared to the theoretical value of the RbLaTa₂O₇ host [i.e., Rb/(La + Ta) = 0.33]. Note that there is a coverage of the CuLTO surface by the organic component.

2.2. Optical Absorption of Samples by UV–Vis Spectroscopy

The optical properties of the RbLTO host and its modified compounds (HLTO, BuALTO, CuLTO, CuLTO-500C, and CuLTO-800R) were studied by UV–Vis spectroscopy (Figure 7A). Moreover, this is a helpful tool to understand the coordination environment of Cu²⁺ ions contained in the lamellar space of the perovskite host.

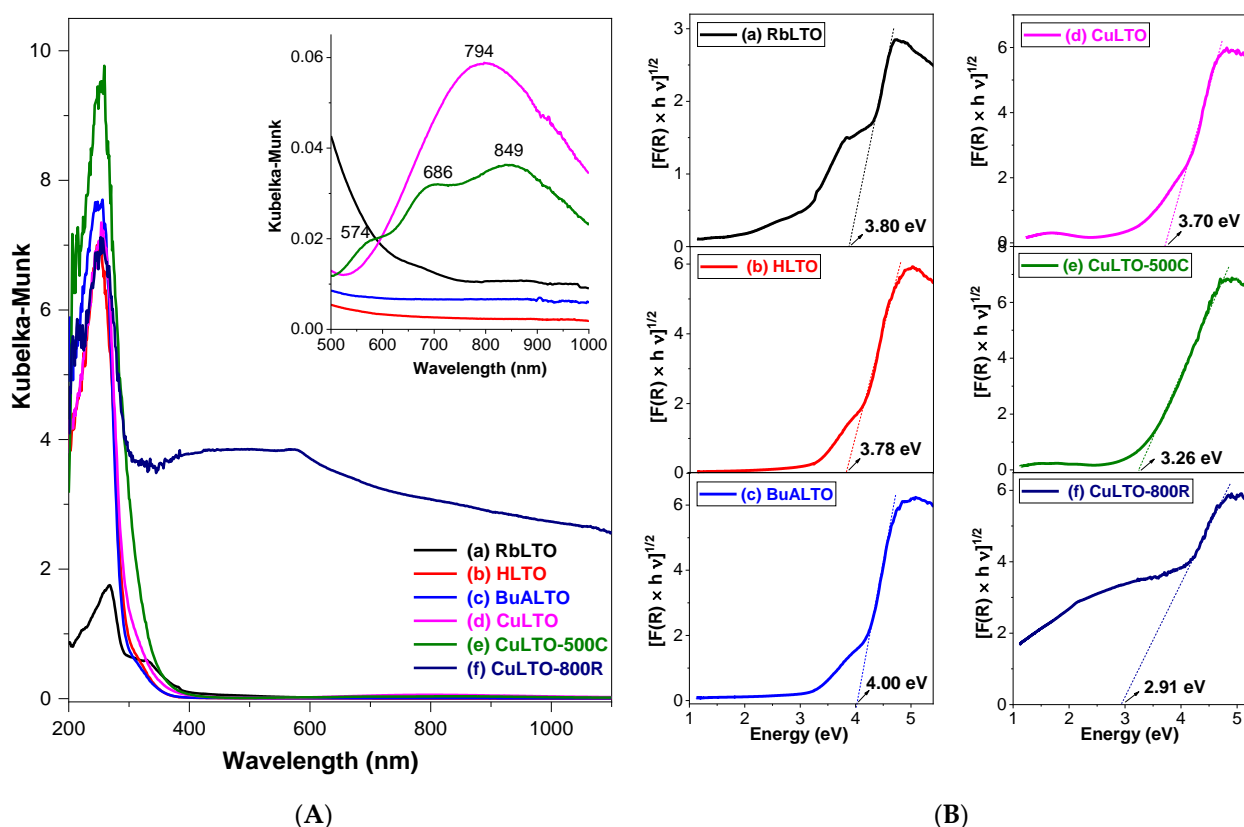



Figure 7. (A) UV-Vis absorption spectra and (B) Tauc plot of the (a) RbLTO, (b) HLTO, (c) BuALTO, (d) CuLTO, (e) CuLTO-500C, and (f) CuLTO-800R.

RbLTO displays an absorption edge at 268 nm with a small shoulder at about 331 nm, corresponding to the electron excitation of the O 2*p* valence band to the Ta 5*d* conduction band. The intercalation of various spacers into the perovskite host layers induces an increase in light absorption. An absorption edge at about 252 nm is observed for the H⁺-, *n*-butylamine-, and Cu²⁺-intercalated perovskites. Notably, copper insertion determines significant changes in UV-Vis spectra in the visible absorption domain (inset of Figure 7A). The CuLTO shows an absorption hump between 520 and 950 nm assigned to the *d-d* electronic transition of Cu²⁺ ions [35]. After calcination at 500 °C, three absorption edges at 573, 686, and 849 nm were perceived. This observation indicates that the copper environment has changed for CuLTO-500C. A reduction at 800 °C leads to a broader and less intense band between 400 and 580 nm in the visible domain.

Different authors claimed that if Cu²⁺ ions are in perfect octahedral coordination, the *d-d* transition band will appear between 750–800 nm. If Cu²⁺ cations are in a distorted octahedral (nearly square planar) configuration, this band will have a blue shift to 600–750 nm. Researchers assigned the broadband between 400 and 450 nm to the charge transfer band for either single- or double-O-bridged copper pairs [36,37].

In line with previous literature studies, it appears that for the CuLTO solid, the Cu²⁺ ion is in perfect octahedral coordination, confidently attributed to the complexation of copper ions with the butyl-amino ligands [38]. After calcination at 500 °C (CuLTO-500C sample), the presence of two Cu²⁺ species could be observed: (i) copper surrounded by amino-ligand and (ii) copper surrounded by oxygen due to surface CuO_x species. A reduction at 800 °C (i.e., CuLTO-800R sample) leads to considerable increases in light absorption compared to the CuLTO and CuLTO-500C solids, which may be due to the charge transfer band for

either the Cu-O-Cu or  pairs and the metallic copper [36,37].

The optical band gap energies (E_g) of all photocatalysts are presented in Figure 7B. The E_g was estimated by Tauc curves corresponding to indirect band transitions. The E_g values of all layered perovskites follow the sequence: CuLTO-800R (2.91 eV) < CuLTO-500C (3.26 eV) < CuLTO (3.70 eV) < HLTO (3.78 eV) < RbLTO (3.80 eV) < BuALTO (4.00 eV). Overall, the RbLaTa₂O₇ host can accommodate various molecules in between layers, enhancing light absorption. The significant decrease in CuLTO-500C and CuLTO-800R band gaps impacts the photocatalytic reaction and the selectivity, as will be seen later.

2.3. Tauc Plot Derived from Photocurrent Spectroscopy (PCS)

A similar method to UV–Vis spectroscopy to estimate the optical band gap of semiconductors is photocurrent spectroscopy. For this purpose, a Tauc plot of $(J_{ph}/\Phi \times h\nu)^n$ versus wavelength was represented, where J_{ph} is the photocurrent, Φ is the photon flux, and n is $\frac{1}{2}$ due to indirect transition [39]. A straight line was fitted at the lower energy region to determine the optical band gap of the layered materials. Figure 8A illustrates the allowed indirect band gap Tauc plots of photoanodes using the normalized photocurrent response. The estimated band gap energies of RbLTO, CuLTO, CuLTO-500C, and CuLTO-800R are 3.51, 3.44, 3.06, and 2.88, respectively. These values imply that the insertion of the copper spacer into the RbLaTa₂O₇ host leads to band-gap shrinking.

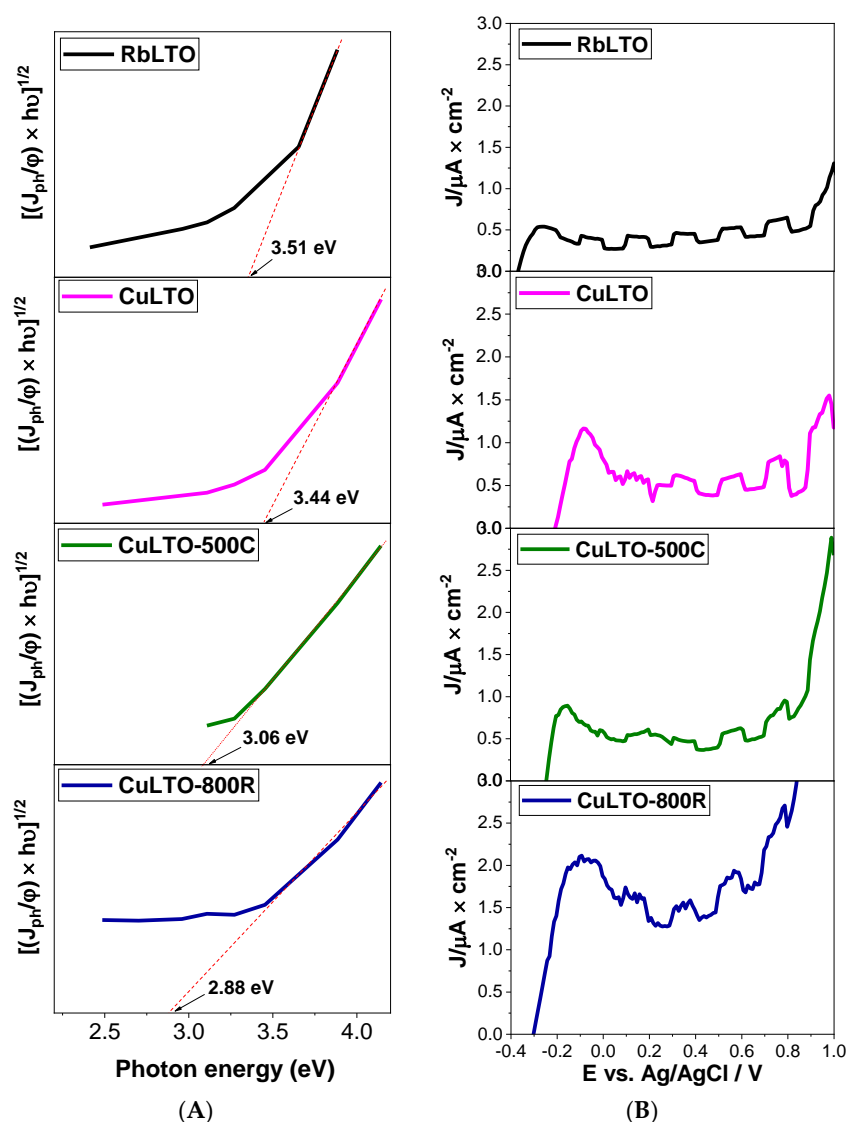


Figure 8. (A) Allowed indirect band gap Tauc plots of RbLTO, CuLTO, CuLTO-500C, and CuLTO-800R photoanodes and (B) LSV plots under chopped AM 1.5 simulated solar light.

The linear sweep voltammetry (LSV) plots under chopped AM 1.5 simulated solar irradiation over RbLTO, CuLTO, CuLTO-500C, and CuLTO-800R photoanodes are compared in Figure 8B. The unmodified RbLTO exhibits the lowest photocurrent density. The LSV response increases for the Cu-modified layered perovskites, while the highest on/off photocurrent response appears on CuLTO-800R. All subjected materials showed a clear characteristic of n-type semiconductors.

2.4. FTIR Absorption Spectra of the Layered Perovskites

The functional groups in RbLaTa₂O₇ original layered perovskite and its spacer-modified compounds were studied by FTIR spectroscopy (Figure 9). In the RbLTO host, the band corresponding to Ta-O-Ta was identified at 550 cm⁻¹. The strong peaks at 613 and 651 cm⁻¹ are due to Ta-O asymmetric stretching vibrations (ν_{as} Ta-O), while the band at 903 cm⁻¹ represents the Ta-O symmetric stretching vibration (ν_s Ta-O) of TaO₆ octahedra [40]. Rb⁺/H⁺ exchange determines one broad band at around 3379 cm⁻¹ and a second one at 1638 cm⁻¹ corresponding to the asymmetric stretching (ν_{as} O-H) and bending mode (δ_s O-H) of hydroxyl groups. The band at 934 cm⁻¹ is related to hydroxyl groups of protonated materials. The protonation step induces a shift to the lower wavenumber of all vibrations related to Ta-O. The introduction of the *n*-butylamine spacer induces important changes in the FTIR spectra of the BuALTO solid. Thus, this sample displays new vibrations allocated to the CH₂ asymmetric stretching band (2964 cm⁻¹), the CH₂ symmetric stretching band (2853 cm⁻¹), and the bending vibrations of the CH₂ groups (1443–1416 cm⁻¹). These bands are abbreviated as ν_{as} CH₂, ν_s CH₂, and δ CH₂, respectively. Additionally, signals of the N-H stretching vibration (3026–3171 cm⁻¹) and the C-N bond (1149–1205 cm⁻¹) are observed [41] confirming the insertion of amine in between the [LaTa₂O₇]⁻ layers. Absorbance below 1000 cm⁻¹ reveals two broad bands at 903 and 804 cm⁻¹ associated with N-H out-of-plane vibration, specific to primary amines [42]. Notably, the band at 903 cm⁻¹ overlaps over the symmetric vibration of Ta-O.

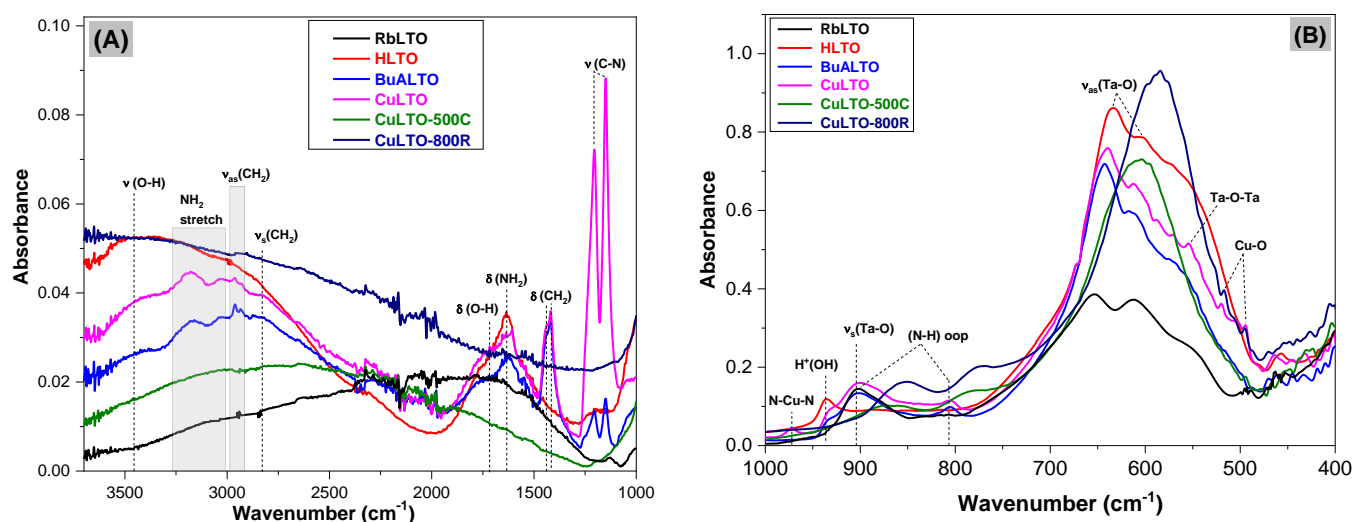


Figure 9. FTIR spectra at the (A) high-wavenumber and (B) low-wavenumber regions for (a) RbLTO, (b) HLTO, (c) BuALTO, (d) CuLTO, (e) CuLTO-500C, and (f) CuLTO-800C.

After Cu²⁺ insertion (CuLTO sample), the signal related to the C-N stretching vibration (1149–1205 cm⁻¹) increases significantly. Alternatively, a new small band develops around 973 cm⁻¹ attributed to N-Cu-N stretching vibration [43]. As a matter of fact, the positively charged Cu²⁺ ions act as a Lewis acid while the (*n*-C₄H₉-NH₃⁺) ligand with one pair of electrons acts as a Lewis base, and consequently, it has a great tendency to form [Cu(NH₂-C₄H₉)₄(H₂O)₂]²⁺ complex. Undeniably, the TG analysis of CuLTO confirms the presence of the [copper-amine] complex. Moreover, the UV-Vis spectra certify the existence of Cu²⁺ in

a perfect octahedron configuration due to the interlayer [Cu-amine] complex. The insertion of spacers determines a redshift of the asymmetric TaO₆ octahedra with 26 cm^{−1} for HLTO, 14 cm^{−1} for BuALTO, and 19 cm^{−1} for CuLTO, respectively, as compared to the RbLTO host. In order to verify the occurrence of interactions between the layered materials and the amine, the FTIR spectrum of neat butylamine is given in the supporting information, Figure S1. It is noticed that the band at 1079–1133 cm^{−1} for both the BuALTO and CuLTO solids is shifted towards higher frequencies compared to neat C₄-amine.

After the different thermal treatments (i.e., calcination/reduction) were applied to a CuLTO fresh sample, all IR bands disappeared in the wavenumbers domain higher than 1000 cm^{−1}. A close view of the FTIR fingerprint domain (Figure 9B) shows the occurrence of new bands at 851 cm^{−1} for CuLTO-500C and 774 cm^{−1} for CuLTO-, compared to the BuALTO and CuLTO samples. It implies that the copper environment has changed in the thermally treated solids. Additionally, the lattice vibration peaks referred to the asymmetric stretching mode of Ta-O converged to one band at 602 cm^{−1} for CuLTO-500C and 585 cm^{−1} for CuLTO-800R. This fact could be attributed to a rearrangement of the interlayer species accompanied by the disordering of the [LaTa₂O₇][−] sheets.

The literature data covering Cu-based materials showed that the bands positioned at 578 cm^{−1} and 435 cm^{−1} are due to ν(Cu-O) [44]. Gopalakrishnan et al. [45] indicate that the Cu-O vibration of Cu₂O nanoparticles appears at about 618 cm^{−1}. Morioka et al. [46] observed small peaks at 428, 503, and 609 cm^{−1} but it has been unclear whether these bands corresponded to CuO and/or Cu₂O. In our preparation, two small bands appear (i) at 495 cm^{−1} for CuLTO, CuLTO-500C, and CuLTO-800R and (ii) at about 516 cm^{−1} for the CuLTO and CuLTO-800R solids. Therefore, this observation witnessed the successful copper spacer insertion into the perovskite structure into the above-stated materials.

2.5. Temperature-Programmed Reduction (TPR) Measurements

To further confirm the successful insertion of a Cu²⁺ spacer into the perovskite galleries, the optical properties were corroborated with those of the H₂-TPR and XPS studies. We focused in particular on the copper chemical state in the assembled Cu-based layered perovskites. The H₂-TPR profiles for CuLTO, CuLTO-500C, and CuLTO-800C catalysts are shown in Figure 10A. The reduction of CuO_x takes place via sequences (Equations (7) and (8)):



All Cu-modified photocatalysts show two distinct regions in the temperature ranges of 50–450 °C and 450–800 °C, respectively. The CuLTO solid displays three separate reduction peaks, with the maxima occurring at 220, 313, and 536 °C, respectively. The first two low-temperature peaks represent the reduction of Cu²⁺ to Cu⁺ and Cu⁺ to Cu⁰ species situated on the catalyst surface [47]. The third large and intense peak is ascribed to the reduction of copper species, (i.e., Cu²⁺ to Cu⁰) located between the perovskite layers [48–50]. Similar results were found by Nestroinaia et al. [51] for Ni-intercalated layered double hydroxide, where the peak between 400–550 °C was attributed to the reduction in Ni³⁺ existing inside brucite-like layers. Hence, the TPR peak at 536 °C of the CuLTO catalyst confidently attests that copper intercalated between the [LaTa₂O₇][−] layers. The calcination treatment over the Cu-fresh solid shifts the reduction peaks towards higher temperature values. Thus, in the TPR profile of the CuLTO-500C, a low-temperature broadened peak is observed along with a high-temperature distinctive one. The broad peak deconvoluted into two peaks was attributed to Cu²⁺/Cu⁺ (280 °C) and Cu⁺/Cu⁰ (448 °C) surface species. The shoulder positioned at 545 °C corresponded to a one-step reduction of Cu²⁺/Cu⁰ interlayer species. The CuLTO-800R material shows a broad peak over the studied temperature range, deconvoluted in four peaks. The low-temperature region (peaks at 194 and 371 °C) indicates the two-step reducibility of surface Cu²⁺. The third peak, centered at 532 °C, is assigned to interlayer copper while the peak at about 650 °C is ascribed to a partial

reduction of some tantalum species in this sample. Previous reports indicated that the reduction of Ta_2O_5 requires temperatures of around $700\text{ }^\circ\text{C}$ [52,53]. This means that the existence of metallic copper in CuLTO-800R solid could promote the reduction of tantalum species at lower temperatures. Generally, the surface Cu^+/Cu^0 redox couple is beneficial for photocatalytic applications relevant to the degradation of organic molecules [54].

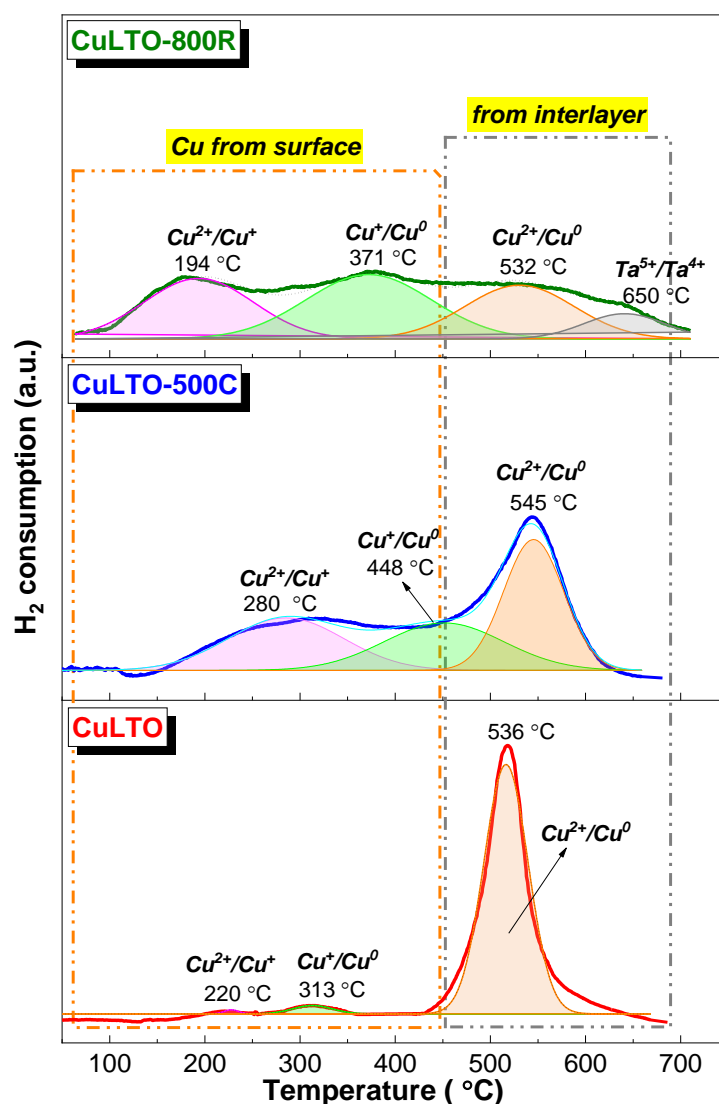


Figure 10. H_2 -TPR profiles of CuLTO, CuLTO-500C, and CuLTO-800R catalysts.

The corresponding H_2 consumption values of Cu-intercalated layered perovskites, expressed in $\mu\text{moles}\cdot\text{g}^{-1}$, are reported in Table 3. For the CuLTO solid, the H_2 consumption by copper localized on the surface of the catalyst is quite small, confirming that the highest amount of copper is located in the interlayer. This observation is in line with the XPS data of CuLTO, which suggests that Cu^{2+} is present as bulk species rather than surface ones, as copper has a weak XPS signal (discussed later in the manuscript). In the case of the CuLTO-500C sample, a higher H_2 consumption value was observed for the copper localized on the surface, accompanied by a slight decrease in the H_2 uptake owing to the interlayer species. For the CuLTO-800R solid, only $66.58\text{ }\mu\text{moles}\cdot\text{g}^{-1}$ of H_2 consumption was calculated for the copper localized into perovskite-like layers. This observation indicates that the reduction process enhanced the migration of interlayer copper particles into highly dispersed surface Cu^+/Cu^0 . The Cu^+/Cu^0 redox couple facilitates the separation of photogenerated carriers, thus improving the photocatalytic reaction [55].

Table 3. H₂ consumptions in H₂-TPR experiments.

Catalyst	H ₂ Consumption ($\mu\text{moles}\cdot\text{g}^{-1}$)			Total H ₂ Consumption ($\mu\text{moles}\cdot\text{g}^{-1}$)
	Cu from Surface		Cu from Interlayer	
	Cu ²⁺ /Cu ⁺	Cu ⁺ /Cu ⁰	Cu ²⁺ /Cu ⁰	
CuLTO	11.64	44.25	662.16	718.05
CuLTO-500C	149.92	140.88	466.61	757.41
CuLTO-800R	91.37	88.54	66.58	246.49

Figure S2 shows the schematic copper species distribution on the surface and into the interlayer of the modified catalysts. Doubtless, in the CuLTO photocatalyst, most of the copper is localized between the galleries, and only a small amount of Cu remains on the catalyst surface. This observation is associated with TG analysis (Figure 3D), which shows that an interlayered [Cu-amine] complex formed in the above-stated sample. When CuLTO was air-calcined at 500 °C, copper species were located both on the surface and interlayer galleries. Indeed, the XRD pattern (Figure 1) validates the appearance of supplementary CuO_x reflexions in CuLTO-500C. For the CuLTO-800R sample, the H₂-TPR study certifies that most of the copper species are emplaced on the catalyst surface, and only a small amount of copper remained in the perovskite layers. Based on these results, a few conclusions are necessary. Between the perovskite galleries, the metal-amine complex bridges the oxygen from the [TaO₆] octahedra. It may be possible that between the layers, there is also Cu²⁺ that comes from the Cu(LaTa₂O₇)₂ crystalline phase. After the calcination process, the decomposition of Cu(LaTa₂O₇)₂ to CuO_x occurs, which migrates onto the catalyst surface. During this process, the decomposition of the [Cu-amine] complex from the interlayer also takes place. When the material is thermally treated at 800 °C in slightly reducing conditions, a higher migration of copper on the catalyst surface occurs.

2.6. XPS Measurements

X-ray photoelectron spectroscopy (XPS) analysis was carried out to further investigate the oxidation state and chemical composition of the newly assembled architectures. Figure 11A shows the XPS spectra of the Cu 2p^{3/2} emission line for the CuLTO, CuLTO-500C, and CuLTO-800R solids. The C 1 s, O 1 s, La 3 d, and Ta 4 f emission lines of the Cu-modified layered perovskites are given in the supporting information, Figures S3 and S4.

The photoelectron profile of the Cu 2p^{3/2} region for the CuLTO fresh solid was very weak. In fact, the H₂-TPR results confirmed that most of the Cu entities are located in the interlayer position for this sample, while the penetration depth for XPS detection is only several nanometers. Notice that the butylamine covered the surface of the above-mentioned sample. This is the reason no detectable copper peak can be observed on its XPS spectra. In CuLTO-500C material, there is a peak at a binding energy of 933.6 eV and a weak shake-up satellite at 943.6 eV. According to literature reports, the binding energy (BE) of Cu 2p^{3/2} related to Cu²⁺ ions ranges between 932.8–933.6 eV (with shake-up satellite features at 940–945 eV) [56,57]. The obtained spectra agree with the literature data, confirming the presence of Cu²⁺ as a major species in the CuLTO-500C solid. After the treatment of CuLTO at 800 °C in a reductive atmosphere, the peak for Cu²⁺ disappeared, and one single peak at 932.8 eV was detected. The results reveal that in the CuLTO-800R solid, copper predominantly existed as Cu⁺ and Cu⁰ species. In line with TPR studies, the reducing conditions lead to a migration of Cu²⁺ from the interlayer space towards the surface of the catalyst in the form of Cu⁺ and metallic copper.

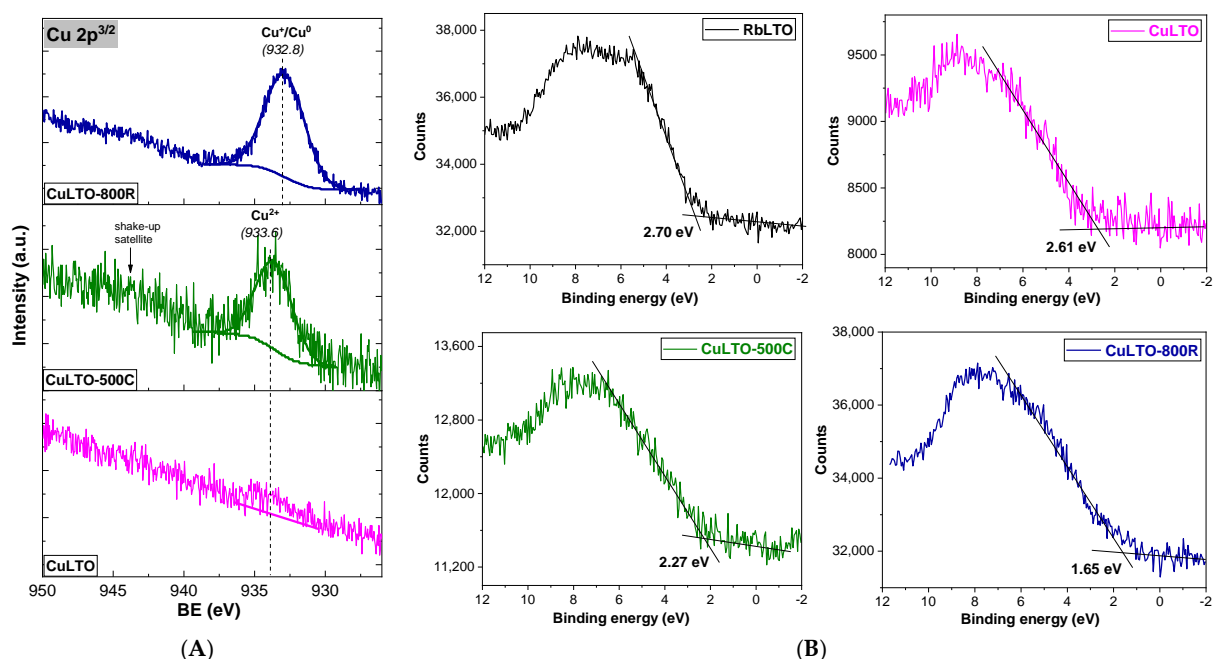


Figure 11. (A) XPS spectra for the $\text{Cu}2p_{3/2}$ emission line of (a) CuLTO, (b) CuLTO-500C, and (c) CuLTO-800R materials, and (B) valence band of unmodified RbLTO and Cu-modified perovskites.

The valence band (VB) spectra of the RbLTO, CuLTO, CuLTO-500C, and CuLTO-800R layered materials were also investigated by the XPS technique (Figure 11B). The VB values of the four samples were obtained by the linear extrapolation of the leading edge to the extended baseline of the VB spectra. Undeniably, copper insertion into the perovskite layered structures leads to the narrowing of the valence band compared to unmodified RbLTO material.

The band gap energy values derived from the UV-Vis, XPS, and photocurrent spectroscopies were compared in Figure 12. The E_g calculated by the three experimental techniques undoubtedly proves that copper intercalation into perovskite layers induces a red band-gap shift.

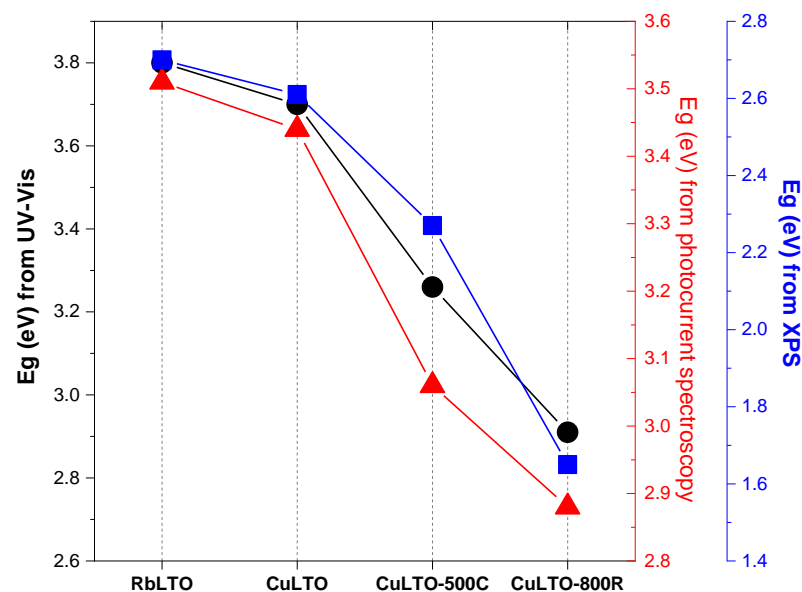


Figure 12. Comparison of the band gap values calculated from UV-Vis, XPS, and photocurrent spectroscopies for the RbLTO, CuLTO, CuLTO-500C, and CuLTO-800R materials.

3. Evaluation of Photocatalytic Activity

The physical features of the synthesized layered perovskites are expected to show different photocatalytic behavior. With this aim, the photodegradation of phenol (Ph) under simulated solar irradiation over the RbLTO, HLTO, CuLTO, CuLTO-500C, and CuLTO-800R photocatalysts was investigated as a model reaction. Table 4 gives the conversion of phenol after 4 h of reaction and the specific surface area over the studied photocatalysts.

Table 4. Photocatalytic results of the tested photocatalysts.

Photocatalyst	Phenol Conversion (%) ¹	SSA (m ² ·g ^{−1})
RbLTO	7.6	1.5
HLTO	8.5	2.6
CuLTO	13.0	4.1
CuLTO-500C	14.9	4.9
CuLTO-800R	16.6	3.4

¹ Phenol conversion after 4 h of reaction time (experimental conditions: 110 mL of 50 mg·L^{−1} phenol aqueous solution, 0.05 g catalyst, T = 18 °C, light source AM 1.5).

The conversion of phenol over an unmodified RbLTO photocatalyst was about 7.6% after 4 h of light irradiation. After Rb⁺ replacement by H⁺, the catalytic performance increased, reaching 8.5% of phenol conversion for the HLTO photocatalyst. The insertion of Cu²⁺ ions in between the [LaTa₂O₇][−] slabs influenced the phenol conversion and its selectivity. The CuLTO photocatalyst improves its activity up to 13.0% phenol conversion after 4 h of reaction time. Additionally, the copper spacer has a beneficial role in the layered perovskite structure by (a) increasing its specific surface area from 1.5 m²·g^{−1} for the RbLTO host up to 4.1 m²·g^{−1} for CuLTO and (b) enhancing the photocatalytic performance for phenol photodegradation. The different thermal treatments applied to the CuLTO fresh solid determine distinct behavior for the photodegradation of phenol. Accordingly, the air-calcination of the CuLTO-500C catalyst led to an increase in phenol conversion by up to 14.9%. On the other hand, the reduced CuLTO-800R catalyst determines the highest conversion of phenol (16.6%) among all studied photocatalysts.

The photocatalytic reaction follows pseudo-first-order kinetics according to the equation $\ln(C/C_0) = -kt$, where C and C_0 designate the phenol concentration at time 0 and time t , and k is the apparent rate constant. Figure 13A shows the plot of $\ln(C_0/C)$ versus the irradiation time for the photocatalytic degradation of phenol over the subjected catalysts. The order of the apparent rate constant k values after 1 h of reaction (Figure 13B) follows the sequence: RbLTO (0.032 min^{−1}) < HLTO (0.063 min^{−1}) < CuLTO (0.091 min^{−1}) < CuLTO-500C (0.111 min^{−1}) < CuLTO-800R (0.133 min^{−1}). These results demonstrate that the introduction of a copper spacer promotes an increase in the reaction rate. The enhanced activity of CuLTO-800R compared to the RbLTO host was favored by its narrow band gap (3.16 eV), as determined from UV-Vis, XPS, and photocurrent spectroscopies. Additionally, the H₂-TPR and XPS measurements confirmed the presence of a Cu⁺/Cu⁰ redox couple localized on the CuLTO-800R catalyst surface, which is responsible for its higher activity.

Very interesting results were perceived for the distribution of the reaction products shown in Figure 13C. Therefore, hydroquinone (HQ) and 1,2-dihydroxybenzene (1,2-DHBZ) were identified as major intermediate products over the RbLTO, HLTO, and CuLTO photocatalysts. Contrarily, both CuLTO-500C and CuLTO-800R photocatalysts lead to the formation of benzoquinone (BQ) as a product intermediate. These results imply that the reaction mechanism is distinct in the Cu-intercalated layered perovskites. Figure 13D shows the catalytic efficiency of phenol mineralization over the RbLTO, HLTO, CuLTO, CuLTO-500C, and CuLTO-800R studied catalysts. The enhanced Cu-modified photocatalysts' activity compared to the RbLTO host is attributed to a better charge separation at the layer/modified interfaces and improved light harvesting ability due to band-gap shrinking. Notice that the CuLTO-800R solid was the most effective photocatalyst regarding the efficiency of phenol mineralization, with 2.82 μmoles·h^{−1} of CO₂ and 1.78 μmoles·h^{−1} of

H₂, respectively. The stability/reusability tests were performed with the catalyst displaying the best performances for the degradation of phenol under identical reaction conditions. The catalyst was recovered after centrifugation, dried, and used for the next run. After three cycling processes (Figure 13E), the degradation efficiency of phenol over CuLTO-800R remained satisfactory. In order to understand the morphological evolution of CuLTO-800R after three photocatalytic runs, SEM and TEM analyses were carried out (Figure S5). Morphological investigation revealed no significant change in the shape of the spent CuLTO-800R catalyst after the reusability test. The good stability of the CuLTO-800R material may be attributed to the more homogeneous dispersion of the Cu atoms within the [LaTa₂O₇][−] network. These observations demonstrate the long-term stability of the CuLTO-800R material.

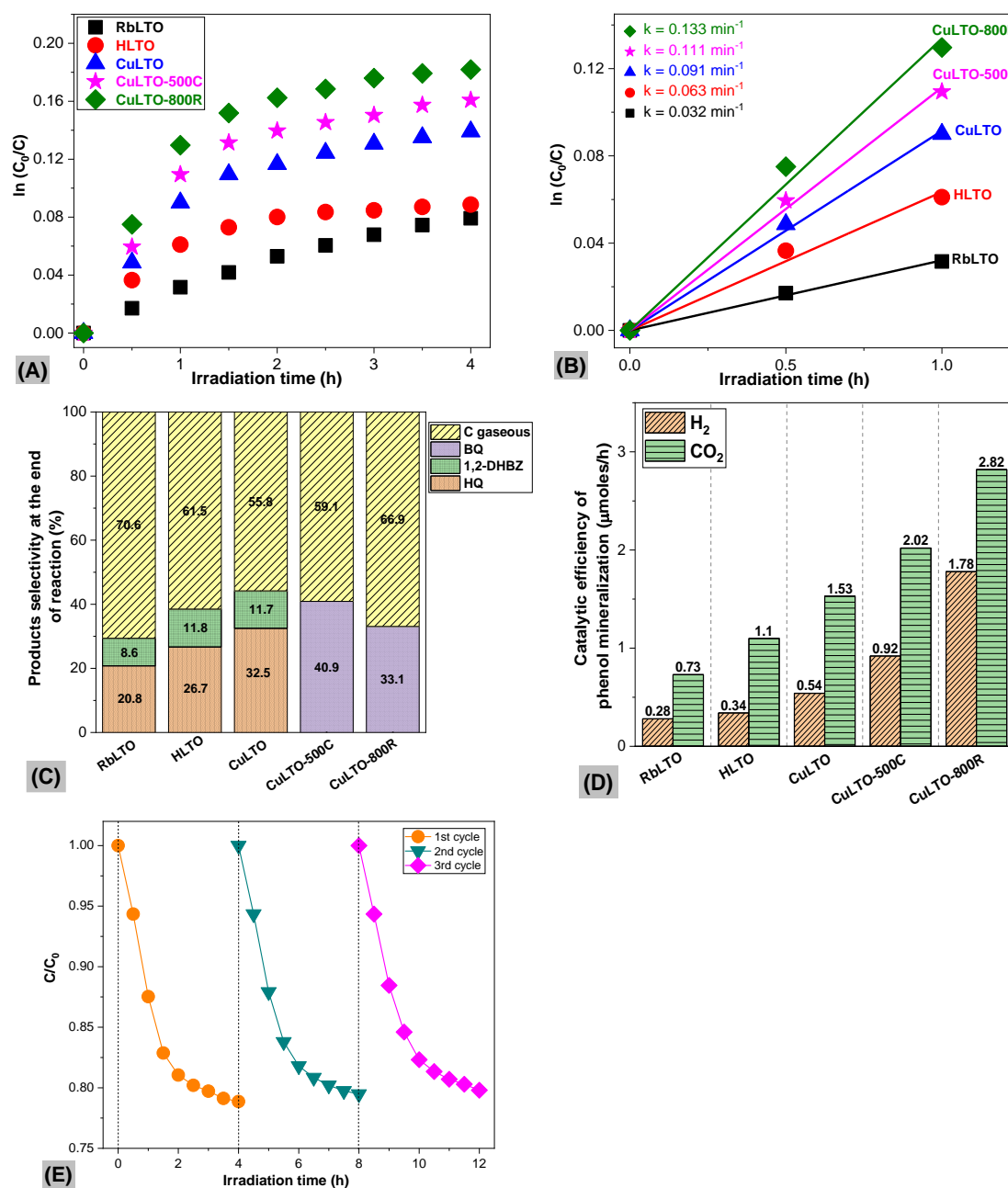


Figure 13. Graphical representation of the (A) pseudo-first-order kinetic plot on photodegradation of phenol, (B) apparent rate constant k (in min^{−1}), (C) the product selectivity at the end of the reaction, (D) the catalytic efficiency of phenol mineralization, and (E) the stability of the CuLTO-800R photocatalyst.

The benefit of copper ion insertion was relevant for the Cu-modified photocatalysts, where the specific surface area (SSA) of CuLTO was $4.1 \text{ m}^2 \cdot \text{g}^{-1}$ (Table 4). This value is about three times larger than that of the $\text{RbLaTa}_2\text{O}_7$ host ($1.5 \text{ m}^2 \cdot \text{g}^{-1}$). Both thermally treated photocatalysts displayed higher SSA against the perovskite host with values of $4.9 \text{ m}^2 \cdot \text{g}^{-1}$ for CuLTO-500C and $3.4 \text{ m}^2 \cdot \text{g}^{-1}$ for CuLTO-800R, respectively. Doubtless, the insertion of various spacers into a layered compound provides original routes for tuning the physicochemical properties of the newly obtained materials.

In order to understand the mechanism, reactive oxygen species (ROS) generation under simulated solar irradiation was investigated according to the previously reported procedure [58]. Figure 14 displays the photogeneration of (A) a hydroxyl radical and (B) a superoxide anion over the CuLTO, CuLTO-500C, and CuLTO-800R photocatalysts. The hydroxyl radical ($\bullet\text{OH}$) occurrence was evaluated based on photoluminescence (PL) emission peaking around 450 nm due to the umbelliferone formation, a coumarine derivative product obtained in the presence of photogenerated hydroxyl radicals. Figure 14A is indicative of the lack of $\bullet\text{OH}$ in the investigated photocatalytic systems, with no significant peaks being perceived around 450 nm. The superoxide anion ($\bullet\text{O}_2^-$) formation under the simulated solar irradiation was evaluated from its interaction with XTT sodium salt, resulting in formazan production, with a characteristic peak appearing in the UV-Vis spectra. According to Figure 14B, only the CuLTO catalyst proves to generate $\bullet\text{O}_2^-$. For the aforementioned sample, a broad band ranging from 420 to 550 nm arises after 20 min of irradiation.

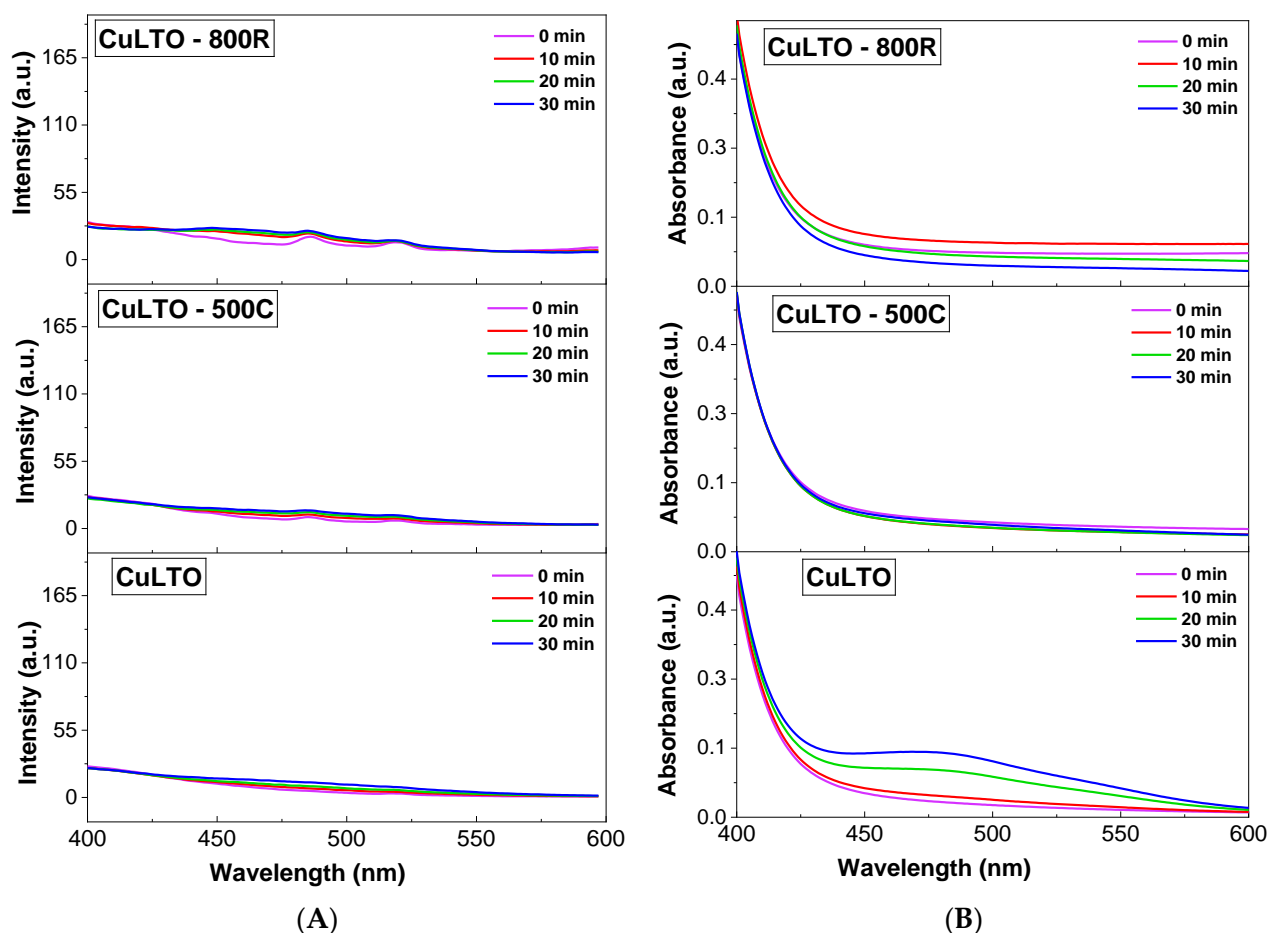


Figure 14. Photogeneration of (A) hydroxyl radical ($\bullet\text{OH}$) and (B) superoxide anion ($\bullet\text{O}_2^-$) over the CuLTO, CuLTO-500C, and CuLTO-800R photocatalysts.

Correlating ROS generation with photocatalytic activity, it is concluded that the reaction mechanism involves the generation of photoinduced electron-hole pairs. For the CuLTO catalysts, the superoxide anion ($\bullet\text{O}_2^-$) consumes the electrons (e^-) generated by irradiation, decreasing the photocatalytic activity. The reaction mechanism of the CuLTO-500C and CuLTO-800R photocatalysts is also produced through e^-/h^+ , but the absence of $\bullet\text{O}_2^-$ is beneficial for the reaction of mineralization. A possible reaction mechanism of Cu-modified perovskites is advanced in Figure 15A.

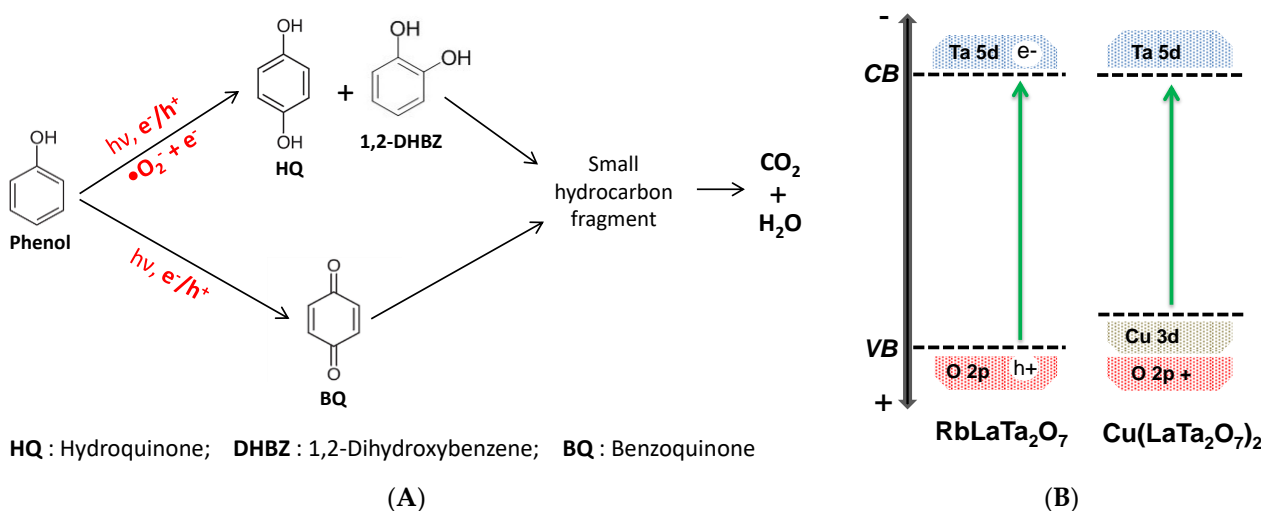


Figure 15. Schematic representation of (A) phenol photocatalytic pathways over Cu-intercalated perovskites, and (B) possible electronic structures of unmodified $\text{RbLaTa}_2\text{O}_7$ and $\text{Cu}(\text{LaTa}_2\text{O}_7)_2$ -modified perovskites.

The photocatalytic degradation of phenol under simulated solar irradiation is an effective example of the degradation of persistent water contaminants [59]. Due to its abundance and low cost, copper is an affordable alternative to expensive noble metals (Au, Ag), widely used in various applications. The p-type CuO_x possesses remarkable properties such as catalytic and antibacterial activities, optoelectronic properties, and high stability [60]. Further, perovskite with a layered structure, such as Bi_2WO_6 , [61,62] demonstrated excellent activity in the mineralization of pollutants under light irradiation due to the transfer of electrons to the surface of the photocatalyst along the layered network. The recombination of charge carriers in such perovskites was depressed by the electron transfer to the layered host.

The advantages of the proposed Cu-modified layered perovskites can be envisaged as a “nanoreactor” where the reactant is confined within a layered perovskite structure in a restricted area, limiting the migration and recombination of photogenerated carriers. From the perspective of the electronic structure of the $\text{RbLaTa}_2\text{O}_7$ perovskite, its valence band (VB) is composed of O 2p orbitals, while the Ta 5d orbitals occupy the conduction band (CB). The Rb and La cations do not directly contribute to a band formation and solely build up the crystal structure of the perovskite. The symmetry of the metal-oxygen octahedral/tetrahedral coordination and the VB and CB structures also play crucial roles in determining the photocatalytic activity [63]. A successful approach to raise the valence band and decrease the band-gap size of the mixed oxides is to combine the elements with d^{10} (i.e., Cu^+ , Ag^+) and d^0 (i.e., Nb^{5+} , Ta^{5+}) electron configurations. In these compounds, the band-gap excitations take place from a metal-to-metal charge transfer (MMCT) transition between electron-donating d^{10} and electron-accepting d^0 configurations [64]. As an example, $\text{Cu}_5\text{Ta}_{11}\text{O}_{30}$ and $\text{Cu}_3\text{Ta}_7\text{O}_{19}$ perovskites displayed a narrower band gap compared to unmodified layered oxides due to an MMCT between the Cu 3d and Ta 5d orbitals [65]. Zhang et al. [66] proposed a practical strategy to fine-tune the energy band structure of new oxynitrides by forming solid solutions between two perovskite-type materials. These

authors reported that the VB of the synthesized materials was formed by N 2p with minor O 2p, while the CB was composed of Ti 3d in the majority and O 2p, La 5d, and N 2p in the minority. Jiang and co-workers [67] found that the electronic structure of γ - $\text{Cu}_3\text{V}_2\text{O}_8$ consisted of O 2p states while the bonding Cu 3d and V 3d states were observed to lie deeper within the valence band. The CB was found to be dominated by unoccupied Cu 3d orbitals, with V 3d states residing at higher energies.

When comparing our results with the findings in prior studies, a similar conclusion was reached. Here, it is postulated that the insertion of a copper spacer modifies the valence band of Cu-based photocatalysts. The narrow band gap of Cu-intercalated perovskites could be attributed to their valence band consisting of a Cu 3d and O 2p orbitals mixture. A possible electronic structure of the $\text{RbLaTa}_2\text{O}_7$ host and its modified $\text{Cu}(\text{LaTa}_2\text{O}_7)_2$ perovskite are proposed in Figure 15B. The current literature on the photocatalytic degradation of phenol admitted that during the reaction, hydroquinone, catechol, and p-benzoquinone are identified as major intermediates. Other reaction intermediate products (chloro-hydroquinone, 4-chlorocatechol, and resorcinol) can eventually be converted into acetylene, maleic acid, CO, and CO_2 . Different mechanisms have been proposed for the photodegradation of organic pollutants, where the hydroxyl radical ($\bullet\text{OH}$), the superoxide radical ($\bullet\text{O}_2^-$), and the hole (h^+) are reviewed as the main reactive species [68]. Trapping experiments carried out on a phosphorus-doped carbon-supported Cu_2O composite [69] indicated that the $\bullet\text{O}_2^-$ radical was the major active species, while the hydroxyl radical played a minor role in the phenol photodegradation. Therefore, the intercalation of copper between the interlayer spaces of perovskite will serve as a promoter for charge separation between electrons and holes, leading to enhancements in the photocatalytic degradation of pollutants. This study shows the great versatility of RbLaTa-based layered perovskite for producing assembled materials with different properties by only controlling the spacer.

4. Materials and Methods

4.1. Synthesis of Catalytic Materials

Preparation of $\text{RbLaTa}_2\text{O}_7$ layered perovskite host. $\text{RbLaTa}_2\text{O}_7$ powder was synthesized by the solid-state route as reported in a previous paper [70]. The stoichiometric amounts of Rb_2CO_3 , La_2O_3 , and Ta_2O_5 with a 50% molar excess of Rb_2CO_3 were treated in an air atmosphere at 1200 °C for 18 h with one intermediate grinding. The obtained white solid was washed with water and air-dried at 110 °C overnight. This sample was designated as RbLTO.

Preparation of HLaTa_2O_7 protonated perovskite. In a typical proton exchange reaction, the starting layered perovskite (1 g) was dispersed in an aqueous solution of 3M HNO_3 (100 mL) and stirred at room temperature for one week, with the daily renewal of the acid solution according to ref. [71]. This solid was labeled as HLTO.

Amine-intercalated layered perovskite. In order to intercalate copper species in between interlayers of the perovskite, the expansion of its interlamellar gallery is needed. Therefore, the HLaTa_2O_7 protonated layered perovskite (0.5 g) was dispersed in a 30 mL *n*-butylamine (BuA)-water mixture (1/1, *v/v*) and heated at 70 °C for 24 h. The white suspension was filtered, washed with acetone and water, and then air-dried at 110 °C overnight. The obtained solid was designated as BuALTO.

Assembling of $\text{Cu}(\text{LaTa}_2\text{O}_7)_2$ novel architecture. For the copper intercalation procedure, the amine-treated powder (0.2 g) was dispersed in an aqueous solution of $\text{Cu}(\text{NO}_3)_2 \cdot 4\text{H}_2\text{O}$ (100 mL, 0.057 M) and kept at 80 °C for 60 h. The resultant mixture was washed with water and air-dried overnight at 110 °C. This solid was designated as CuLTO.

To further investigate the nature and localization of the copper spacer in the novel layered architecture, the CuLTO fresh solid was subjected to different thermal treatments, as follows: (i) calcination in an air atmosphere at 500 °C for 2 h (sample labeled as CuLTO-500C) and (ii) reduction at 800 °C in a 5% H_2/Ar atmosphere for 2 h (sample denoted as CuLTO-800R).

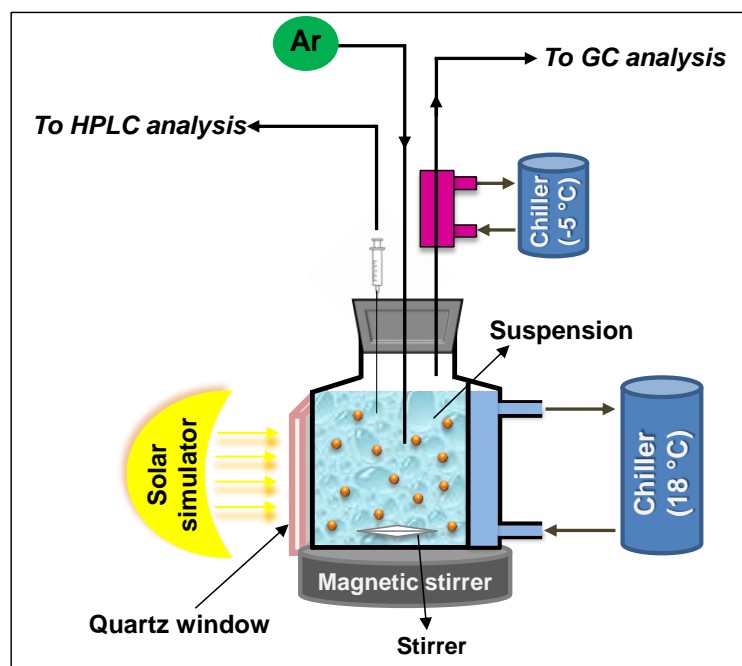
4.2. Characterization of Photocatalysts

The $\text{RbLaTa}_2\text{O}_7$ original layered perovskite and its corresponding intercalated-guest spacers were characterized by various techniques. X-ray diffraction (XRD) patterns were obtained on a Rigaku Corporation Ultima IV diffractometer, Tokyo, Japan (monochromatized $\text{Cu K}\alpha$ ($\lambda = 0.15418$ nm)). The average crystallite size was calculated using the Debye-Scherrer equation. The X-ray photoelectron microscopy (XPS) experiments were carried out on a SPECS spectrometer, Berlin, Germany with a PHOIBOS 150 analyzer, using non-monochromatic $\text{Al K}\alpha$ radiation (1486.7 eV). The charge compensation was realized by a flood gun of Specs FG15/40 type. The acquisition was operated at a pass energy of 20 eV for the individual spectral lines and 50 eV for the extended spectra. SEM pictures were collected with a high-resolution microscope, an FEI Quanta3D FEG device, Brno, Czech Republic, at an accelerating voltage of 5 kV, in high-vacuum mode with an Everhart-Thornley secondary electron (SE) detector coupled with EDX (energy dispersive X-ray) analysis. TEM micrographs were obtained on a JEM-1400 apparatus, (JEOL Ltd., Tokyo, Japan) operated at 100 kV. The Rb leaching during the protonation step was checked by ion chromatography (Dionex ICS 900, Sunnyvale, CA, USA) through the dosing of Rb^+ cations. Nitrogen BET-specific surface areas were measured at 77 K with a Micromeritics ASAP 2020 instrument, Norcross, GA, USA. Thermo-differential analyses (TG/DTA/DTG) were recorded with Mettler Toledo TGA/SDTA 851^e apparatus (Greifensee, Switzerland) in an air atmosphere using an alumina crucible between 25–1000 °C at a heating rate of 10 °C·min^{−1}. Infrared spectra were obtained in transmission mode using a JASCO spectrophotometer, Tokyo, Japan. UV-Vis spectra were acquired on a Perkin Elmer Lambda 35 spectrophotometer, Shelton, CT, USA equipped with an integrating sphere. The reflectance was converted to absorption using the Kubelka-Munk function. The optical band gap of the samples was calculated according to the formula, E_g (eV) = 1240/ λ (wavelength in nm). The temperature-programmed reduction measurements (H_2 -TPR) were performed using a CHEMBET-3000 Quantachrome Instrument, Boynton Beach, FL, USA equipped with a thermal conductivity detector (TCD). In a typical experiment, the fresh sample (0.050 g) was heated up to 800 °C at the constant rate of 10 °C·min^{−1} of the 5 vol.% H_2/Ar reduction gas and a flow rate of 70 mL·min^{−1}. The hydrogen consumption was estimated from the area of the recorded peaks. The calibration of the TCD signal was performed by injecting a known quantity of hydrogen (typically 50 μL) into the carrier gas (Ar). The experimentally obtained peak surface ($\text{mV}\cdot\text{s}$) was thus converted into micromoles of hydrogen. The photoelectrochemical measurements were carried out in an electrochemical cell equipped with a quartz window using a three-electrode configuration. All measurements were performed on a Zahner IM6 potentiostat, Zahner-Elektrik GmbH, Kronach-Gundelsdorf, Germany. A deaerated solution of 0.1 M Na_2SO_4 was used as an electrolyte. The counter electrode was a high-surface Pt wire, and the reference electrode was Ag/AgCl. The working electrode (geometric area of ~ 3.5 cm²) was prepared by the deposition of the interest powder (0.010 g) onto the transparent conductive (TCO) glass (Solaronix, Aubonne, Switzerland). Linear sweep voltammetry (LSV) was carried out at a 10 mV/s rate under chopped AM 1.5 simulated solar light (Pecell-L01, Yokohama, Japan).

4.3. Photocatalytic Degradation of Phenol under Simulated Solar Irradiation

Photocatalytic test. The photocatalytic degradation experiments were performed in a batch photoreactor thermostated at 18 °C (Scheme 2). The AM 1.5 light beam was provided by a solar light simulator (Pecell-L01, Yokohama, Japan) equipped with a 150 W short-arc Xe lamp (1000·W·m^{−2}). The photocatalyst powder (0.05 g) was suspended in 110 mL of 50 mg·L^{−1} aqueous phenol solution. During tests, the Ar carrier gas (10 mL·min^{−1}) was continuously purged into the reaction solution and passed through a refrigerant cooled to −5 °C. This cooler helped to remove the liquid vapors from entering the GC equipment. The photoreactor was provided with a quartz window of 4.5 × 4.5 cm² for light irradiation. Prior to each experiment, the suspension was kept in dark conditions for 30 min under

stirring to attain the adsorption-desorption equilibrium. Subsequently, the reaction vessel was exposed to simulated solar light for 4 h of reaction time.



Scheme 2. Schematic diagram of the experimental setup used for the photocatalytic degradation of phenol under simulated solar light.

Analytical methods. Phenol and intermediate ring compounds (i.e., hydroquinone, benzoquinone, 1,2-dihydroxibenzene) were identified and quantified by high-performance liquid chromatography (HPLC) (Waters, Alliance e2659, Milford, MA, USA) equipped with a UV–Vis detector (Waters, model 2489) ($\lambda = 273$ nm) and a Kromasil 100 5-C18 column. Aliquots of 2 mL of the reaction mixture were collected at 30 min time intervals, filtered through 0.22 μm Q-Max membrane filter, and analyzed by HPLC. The mobile phase was a mixture of Milli-Q water and methanol (50/50, *v/v*) applied in the isocratic elution program. The flow rate of the mobile phase was 1 $\text{mL}\cdot\text{min}^{-1}$, and the injection volume was set to 2 μL . The evolved gases were analyzed every 30 min using online gas chromatography (Buck Scientific, Norwalk, CT, USA) equipped with a TCD detector. The H_2 and O_2 were separated and quantified on Molecular Sieve 5 Å, whereas CO_2 was on the Haysep column.

Reactive oxygen species (ROS) generation. For the hydroxyl radical ($\bullet\text{OH}$) trapping, an amount of 0.001 g catalyst was suspended in 10 mM coumarin (Merck, Darmstadt, Germany) solution and exposed to simulated solar irradiation (Peccel-L01 Solar Simulator, Yokohama, Japan). The formation of a fluorescent product from coumarin interaction with the photogenerated hydroxyl radicals is investigated with a Carry Eclipse fluorescence spectrometer (Agilent Technologies, Santa Clara, CA, USA) for $\lambda_{\text{exc}} = 330$ nm. Superoxide anion ($\bullet\text{O}_2^-$) monitoring was performed by suspending 0.003 g of catalyst in a 3 mM solution of 2,3-Bis(2-methoxy-4-nitro-5-sulphophenyl)-2H-tetrazolium-5-carboxanilide (XTT sodium salt). The XTT formazan appears as a result of XTT interaction with the photogenerated $\bullet\text{O}_2^-$ and generates a broad peak around 470 nm depicted with a UV–Vis spectrophotometer (Analytik Jena Specord 200 Plus, Jena, Germany).

5. Conclusions

A multi-step ion-exchange methodology has been exploited by exchanging Rb^+ with a much smaller Cu^{2+} spacer in the $\text{RbLaTa}_2\text{O}_7$ host to achieve photocatalysts capable of wastewater depollution. The XRD patterns revealed that the interlayer distance of the lamellar perovskites was spacer-related. The UV–Vis, XPS, and photocurrent spectroscopies

demonstrated band-gap narrowing after copper intercalation. The H₂-TPR results indicated that the Cu species located on the surface were reduced at a lower temperature while those from the interlayer occurred at higher temperature ranges. Cu-modified layered perovskites exhibited enhanced photocatalytic activity compared to the RbLaTa₂O₇ host. Experiments proved that the reaction mechanism over Cu-intercalated perovskites was produced via the generation of photoinduced e[−]/h⁺ pairs. The superior photocatalytic activity of CuLTO-800R was attributed to its narrow band gap and photogenerated-carriers separation. Cu-based architectures are promising materials because of their stable perovskite-like slabs and flexible interlayer galleries that facilitate modification.

Supplementary Materials: The following supporting information can be downloaded at: <https://www.mdpi.com/article/10.3390/catal12121529/s1>. Figure S1: FTIR spectra of neat *n*-butylamine; Figure S2: Copper species distribution in CuLTO, CuLTO-500C, and CuLTO-800R catalysts; Figure S3: XPS spectra of (a) RbLTO, (b) CuLTO, (c) CuLTO-500C, and (d) CuLTO-800R layered architectures for C 1s and O 1s emission lines; Figure S4: XPS spectra of (a) RbLTO, (b) CuLTO, (c) CuLTO-500C, and (d) CuLTO-800R layered architectures for La 3d and Ta 4f emission lines; Figure S5: (A) SEM and (B) TEM images of CuLTO-800R photocatalyst after the stability/reusability test; Table S1: Mass loss at different steps of TG curves of all layered perovskite materials. References [32,71,72] are cited in the supplementary materials.

Author Contributions: Conceptualization, I.B.; methodology, I.B., F.P. and M.R.; validation, I.B. and F.P.; investigation, M.R., C.A., F.P., I.A., C.N., D.-I.E., D.C.C., A.M., V.B., J.P.-C., C.M., G.D. and A.S.; resources, I.B. and F.P.; writing—original draft preparation, M.R.; writing—review and editing, I.B. and F.P.; supervision, I.B.; project administration, I.B., F.P. and C.B.; funding acquisition, C.B. and F.P. All authors have read and agreed to the published version of the manuscript.

Funding: This research was funded by the MINISTRY OF RESEARCH, INNOVATION, AND DIGITIZATION, CNCS/CCCDI-UEFISCDI, grant number PN-III-P2-2.1-PTE-2019-0222, within PNC DI III.

Data Availability Statement: All data are available upon reasonable request from the authors.

Conflicts of Interest: The authors declare no conflict of interest. The funders had no role in the design of the study; in the collection, analyses, or interpretation of data; in the writing of the manuscript; or in the decision to publish the results.

References

1. Fang, M.; Kim, C.H.; Mallouk, T.E. Dielectric Properties of the Lamellar Niobates and Titanoniobates AM₂Nb₃O₁₀ and ATiNbO₅ (A = H, K, M = Ca, Pb), and Their Condensation Products Ca₄Nb₆O₁₉ and Ti₂Nb₂O₉. *Chem. Mater.* **1999**, *11*, 1519–1525. [\[CrossRef\]](#)
2. Liu, Y.; Mao, Z.-Q. Unconventional superconductivity in Sr₂RuO₄. *Phys. C Supercond. Appl.* **2015**, *514*, 339–353. [\[CrossRef\]](#)
3. Ida, S.; Ogata, C.; Eguchi, M.; Youngblood, W.J.; Mallouk, T.E.; Matsumoto, Y. Photoluminescence of Perovskite Nanosheets Prepared by Exfoliation of Layered Oxides, K₂Ln₂Ti₃O₁₀, KLnNb₂O₇, and RbLnTa₂O₇ (Ln: Lanthanide Ion). *J. Am. Chem. Soc.* **2008**, *130*, 7052–7059. [\[CrossRef\]](#) [\[PubMed\]](#)
4. Hu, Y.; Mao, L.; Guan, X.; Tucker, K.A.; Xie, H.; Wu, X.; Shi, J. Layered perovskite oxides and their derivative nanosheets adopting different modification strategies towards better photocatalytic performance of water splitting. *Renew. Sustain. Energy Rev.* **2020**, *119*, 109527. [\[CrossRef\]](#)
5. Oshima, T.; Yokoi, T.; Eguchi, M.; Maeda, K. Synthesis and photocatalytic activity of K₂CaNaNb₃O₁₀, a new Ruddlesden-Popper phase layered perovskite. *Dalton Trans.* **2017**, *46*, 10594–10601. [\[CrossRef\]](#) [\[PubMed\]](#)
6. Atri, S.; Tomar, R. A Review on the Synthesis and Modification of Functional Inorganic-Organic-Hybrid Materials via Microwave-Assisted Method. *ChemistrySelect* **2021**, *6*, 9351–9362. [\[CrossRef\]](#)
7. Machida, M.; Yabunaka, J.-I.; Kijima, T. Synthesis and Photocatalytic Property of Layered Perovskite Tantalates, RbLnTa₂O₇ (Ln = La, Pr, Nd, and Sm). *Chem. Mater.* **2000**, *12*, 812–817. [\[CrossRef\]](#)
8. Sanjaya Ranmohotti, K.G.; Josepha, E.; Choi, J.; Zhang, J.; Wiley, J.B. Topochemical Manipulation of Perovskites: Low-Temperature Reaction Strategies for Directing Structure and Properties. *Adv. Mater.* **2011**, *23*, 442–460. [\[CrossRef\]](#)
9. Wang, B.; Dong, X.; Pan, Q.; Cheng, Z.; Yang, Y. Intercalation behavior of *n*-alkylamines into an A-site defective layered perovskite H₂W₂O₇. *J. Solid State Chem.* **2007**, *180*, 1125–1129. [\[CrossRef\]](#)
10. Uppuluri, R.; Gupta, A.S.; Rosas, A.S.; Mallouk, T.E. Soft chemistry of ion-exchangeable layered metal oxides. *Chem. Soc. Rev.* **2018**, *47*, 2401–2430. [\[CrossRef\]](#) [\[PubMed\]](#)
11. Funatsu, A.; Taniguchi, T.; Tokita, Y.; Murakami, T.; Nojiri, Y.; Matsumoto, Y. Nd³⁺-doped perovskite nanosheets with NIR luminescence. *Mater. Lett.* **2014**, *114*, 29–33. [\[CrossRef\]](#)

12. Timmerman, M.A.; Xia, R.; Le, P.T.P.; Wang, Y.; ten Elshof, J.E. Metal Oxide Nanosheets as 2D Building Blocks for the Design of Novel Materials. *Chem. A Eur. J.* **2020**, *26*, 9084–9098. [\[CrossRef\]](#) [\[PubMed\]](#)
13. Li, F.; Xie, Y.; Hu, Y.; Long, M.; Zhang, Y.; Xu, J.; Qin, M.; Lu, X.; Liu, M. Effects of alkyl chain length on crystal growth and oxidation process of two dimensional tin halide perovskites. *ACS Energy Lett.* **2020**, *5*, 1422–1429. [\[CrossRef\]](#)
14. Minich, I.A.; Silyukov, O.I.; Gak, V.V.; Borisov, E.V.; Zvereva, I.A. Synthesis of organic-inorganic hybrids based on perovskite-like bismuth titanate $\text{H}_2\text{K}_{0.5}\text{Bi}_{2.5}\text{Ti}_4\text{O}_{13} \cdot \text{H}_2\text{O}$ and *n*-alkylamines. *ACS Omega* **2020**, *5*, 8158–8168. [\[CrossRef\]](#)
15. Fan, L.; Wei, Y.; Cheng, Y.; Huang, Y.; Hao, S.; Wu, J. Preparation and photocatalytic properties of $\text{HLaNb}_2\text{O}_7/(\text{Pt}, \text{TiO}_2)$ perovskite intercalated nanomaterial. *Int. J. Hydrog. Energy* **2014**, *39*, 7747–7752. [\[CrossRef\]](#)
16. Wu, J.; Cheng, Y.; Lin, J.; Huang, Y.; Huang, M.; Hao, S. Fabrication and photocatalytic properties of $\text{HLaNb}_2\text{O}_7/(\text{Pt}, \text{Fe}_2\text{O}_3)$ pillared nanomaterial. *J. Phys. Chem. C* **2007**, *111*, 3624–3628. [\[CrossRef\]](#)
17. Ebina, Y.; Sakai, N.; Nagasaki, T. Photocatalyst of lamellar aggregates of RuO_x -loaded perovskite nanosheets for overall water splitting. *J. Phys. Chem. B* **2005**, *109*, 17212–17216. [\[CrossRef\]](#)
18. Oshima, T.; Wang, Y.; Lu, D.; Yokoi, T.; Maeda, K. Photocatalytic overall water splitting on Pt nanocluster-intercalated, restacked $\text{KCa}_2\text{Nb}_3\text{O}_{10}$ nanosheets: The promotional effect of co-existing ions. *Nanoscale Adv.* **2019**, *1*, 189–194. [\[CrossRef\]](#)
19. Jiang, C.; Moniz, S.J.A.; Wang, A.; Zhang, T.; Tang, J. Photoelectrochemical devices for solar water splitting-materials and challenges. *Chem. Soc. Rev.* **2017**, *46*, 4645–4660. [\[CrossRef\]](#)
20. Majumdar, D.; Ghosh, S. Recent advancements of copper oxide based nanomaterials for supercapacitor applications. *J. Energy Storage* **2021**, *34*, 101995. [\[CrossRef\]](#)
21. Wang, Q.; Domen, K. Particulate photocatalysts for light-driven water splitting: Mechanisms, challenges, and design strategies. *Chem. Rev.* **2020**, *120*, 919–985. [\[CrossRef\]](#) [\[PubMed\]](#)
22. Watanabe, K.; Iwashina, K.; Iwase, A.; Nozawa, S.; Adachi, S.-I.; Kudo, A. New Visible-Light-Driven H_2 - and O_2 -Evolving Photocatalysts Developed by Ag(I) and Cu(I) Ion Exchange of Various Layered and Tunneling Metal Oxides Using Molten Salts Treatments. *Chem. Mater.* **2020**, *32*, 10524–10537. [\[CrossRef\]](#)
23. Iwashina, K.; Iwase, A.; Kudo, A. Sensitization of wide band gap photocatalysts to visible light by molten CuCl treatment. *Chem. Sci.* **2015**, *6*, 687–692. [\[CrossRef\]](#)
24. Wysocka, I.; Kowalska, E.; Trzciński, K.; Łapiński, M.; Nowaczyk, G.; Zielińska-Jurek, A. UV-Vis-Induced Degradation of Phenol over Magnetic Photocatalysts Modified with Pt, Pd, Cu and Au Nanoparticles. *Nanomaterials* **2018**, *8*, 28. [\[CrossRef\]](#) [\[PubMed\]](#)
25. Cordova Villegas, L.G.; Mashhadi, N.; Chen, M.; Mukherjee, D.; Taylor, K.E.; Biswas, N. A Short Review of Techniques for Phenol Removal from Wastewater. *Curr. Pollut. Rep.* **2016**, *2*, 157–167. [\[CrossRef\]](#)
26. Alonso, J.A.; Martínez-Lope, M.J.; Casais, M.T.; Fernández-Díaz, M.T. Evolution of the Jahn–Teller Distortion of MnO_6 Octahedra in RMnO_3 Perovskites ($\text{R} = \text{Pr}, \text{Nd}, \text{Dy}, \text{Tb}, \text{Ho}, \text{Er}, \text{Y}$): A Neutron Diffraction Study. *Inorg. Chem.* **2000**, *39*, 917–923. [\[CrossRef\]](#)
27. Hyeon, K.-A.; Byeon, S.-H. Synthesis and Structure of New Layered Oxides, $\text{M}^{\text{II}}\text{La}_2\text{Ti}_3\text{O}_{10}$ ($\text{M} = \text{Co}, \text{Cu}, \text{and Zn}$). *Chem. Mater.* **1998**, *11*, 352–357. [\[CrossRef\]](#)
28. Ogawa, M.; Kuroda, K. Preparation of Inorganic-Organic Nanocomposites through Intercalation of Organoammonium Ions into Layered Silicates. *Bull. Chem. Soc. Jpn.* **1997**, *70*, 2593–2618. [\[CrossRef\]](#)
29. Sasaki, T.; Kooli, F.; Iida, M.; Michiue, Y.; Takenouchi, S.; Yajima, Y.; Izumi, F.; Chakoumakos, B.C.; Watanabe, M. A Mixed Alkali Metal Titanate with the Lepidocrocite-like Layered Structure. Preparation, Crystal Structure, Protonic Form, and Acid–Base Intercalation Properties. *Chem. Mater.* **1998**, *10*, 4123–4128. [\[CrossRef\]](#)
30. Sasaki, T.; Izumi, F.; Watanabe, M. Intercalation of Pyridine in Layered Titanates. *Chem. Mater.* **1996**, *8*, 777–782. [\[CrossRef\]](#)
31. Sun, C.; Peng, P.; Zhu, L.; Zheng, W.; Zhao, Y. Designed Reversible Alkylamine Intercalation-Deintercalation in the Layered Perovskite-Type Oxide $\text{KCa}_2\text{Nb}_3\text{O}_{10}$. *Eur. J. Inorg. Chem.* **2008**, *24*, 3864–3870. [\[CrossRef\]](#)
32. Raciutele, M.; Papa, F.; Culita, D.C.; Munteanu, C.; Atkinson, I.; Bratan, V.; Pandeale-Cusu, J.; State, R.; Balint, I. Impact of $\text{RbLaTa}_2\text{O}_7$ Layered Perovskite Synthesis Conditions on their Activity for Photocatalytic Abatement of Trichloroethylene. *Rev. Roum. Chim.* **2018**, *63*, 821–828.
33. Geselbracht, M.J.; White, H.K.; Blaine, J.M.; Diaz, M.J.; Hubbs, J.L.; Adelstein, N.; Kurzman, J.A. New solid acids in the triple-layer Dion-Jacobson layered perovskite family. *Mater. Res. Bull.* **2011**, *46*, 398–406. [\[CrossRef\]](#)
34. Cheng, S.; Hwang, H.-D.; Maciel, G.E. Synthesis and pillaring of a layered vanadium oxide from V_2O_5 at ambient temperature. *J. Mol. Struct.* **1998**, *470*, 135–149. [\[CrossRef\]](#)
35. Castellini, E.; Bernini, F.; Sebastianelli, L.; Sainz-Díaz, C.I.; Serrano, A.; Castro, G.R.; Malferrari, D.; Brigatti, M.F.; Borsari, M. Interlayer-Confined Cu(II) Complex as an Efficient and Long-Lasting Catalyst for Oxidation of H_2S on Montmorillonite. *Minerals* **2020**, *10*, 510. [\[CrossRef\]](#)
36. Mokhtar, A.; Medjhoula, Z.A.K.; Djelad, A.; Boudia, A.; Bengueddach, A.; Sassi, M. Structure and intercalation behavior of copper II on the layered sodium silicate magadiite material. *Chem. Pap.* **2018**, *72*, 39–50. [\[CrossRef\]](#)
37. Ding, Z.; Frost, R.L. Study of copper adsorption on montmorillonites using thermal analysis methods. *J. Colloid Interface Sci.* **2004**, *269*, 296–302. [\[CrossRef\]](#) [\[PubMed\]](#)
38. Hakiki, A.; Kerbadou, R.M.; Boukoussa, B.; Zahmani, H.H.; Launay, F.; Pailleret, A.; Pillier, F.; Hacini, S.; Bengueddach, A.; Hamacha, R. Catalytic behavior of copper-amine complex supported on mesoporous silica SBA-15 toward mono-Aza-Michael addition: Role of amine groups. *J. Inorg. Organomet. Polym. Mater.* **2019**, *29*, 1773–1784. [\[CrossRef\]](#)

39. Chen, Z.; Deutsch, T.G.; Dinh, H.N.; Domen, K.; Emery, K.; Forman, A.J.; Gaillard, N.; Garland, R.; Heske, C.; Jaramillo, T.F.; et al. Photoelectrochemical Water Splitting. Incident photon-to-current efficiency and photocurrent spectroscopy. In *Photoelectrochemical Water Splitting*; Chen, Z., Dinh, H.N., Miller, E., Eds.; Briefs in Energy; Springer: New York, NY, USA, 2013; pp. 87–97. [\[CrossRef\]](#)
40. Ghosh, B.; Halder, S.; Sinha, T.P. Dielectric Relaxation and Collective Vibrational Modes of Double-Perovskites A_2SmTaO_6 ($A = Ba, Sr$ and Ca). *J. Am. Ceram. Soc.* **2014**, *97*, 2564–2572. [\[CrossRef\]](#)
41. Kumar, D.V.R.; Kim, I.; Zhong, Z.; Kim, K.; Lee, D.; Moon, J. Cu(II)-alkyl amine complex mediated hydrothermal synthesis of Cu nanowires: Exploring the dual role of alkyl amines. *Phys. Chem. Chem. Phys.* **2014**, *16*, 22107–22115. [\[CrossRef\]](#)
42. Espeel, P.; Goethals, F.; Driessen, F.; Nguyen, L.-T.T.; Du Prez, F.E. One-pot, additive-free preparation of functionalized polyurethanes via amine-thiol-ene conjugation. *Polym. Chem.* **2013**, *4*, 2449–2456. [\[CrossRef\]](#)
43. Du, J.; Zhao, Y.; Chen, J.; Zhang, P.; Gao, L.; Wang, M.; Cao, C.; Wen, W.; Zhu, C. Difunctional Cu-doped carbon dots: Catalytic activity and fluorescence indication for the reduction reaction of p-nitrophenol. *RSC Adv.* **2017**, *7*, 33929–33936. [\[CrossRef\]](#)
44. Fang, L.; Dong, S.; Shi, L.; Sun, Q. Modification of $CuCl_2 \cdot 2H_2O$ by dielectric barrier discharge and its application in the hydroxylation of benzene. *New J. Chem.* **2019**, *43*, 12744–12753. [\[CrossRef\]](#)
45. Gopalakrishnan, K.; Ramesh, C.; Ragunathan, V.; Thamilselvan, M.; Thamilselvan, M. Antibacterial activity of Cu_2O nanoparticles on *E. coli* synthesized from *Tridax procumbens* leaf extract and surface coating with polyaniline. *Dig. J. Nanomater. Biostruct.* **2012**, *7*, 833–839.
46. Morioka, T.; Takesue, M.; Hayashi, H.; Watanabe, M.; Smith, R.L. Antioxidation properties and surface interactions of polyvinylpyrrolidone-capped zerovalent copper nanoparticles synthesized in supercritical water. *ACS Appl. Mater. Interfaces* **2016**, *8*, 1627–1634. [\[CrossRef\]](#) [\[PubMed\]](#)
47. Torre-Abreu, C.; Ribeiro, M.F.; Henriques, C.; Delahay, G. The role of Si/Al ratio, copper content and co-cation. *Appl. Catal. B Environ.* **1997**, *14*, 261–272. [\[CrossRef\]](#)
48. Wang, Z.; Yan, X.; Bi, X.; Wang, L.; Zhang, Z.; Jiang, Z.; Xiao, T.; Umar, A.; Wang, Q. Lanthanum-promoted copper-based hydrotalcites derived mixed oxides for NO_x adsorption, soot combustion and simultaneous NO_x -soot removal. *Mater. Res. Bull.* **2014**, *51*, 119–127. [\[CrossRef\]](#)
49. Gervasini, A.; Bennici, S. Dispersion and surface states of copper catalysts by temperature-programmed-reduction of oxidized surfaces (s-TPR). *Appl. Catal. A Gen.* **2005**, *281*, 199–205. [\[CrossRef\]](#)
50. Zeng, Y.; Wang, T.; Zhang, S.; Wang, Y.; Zhong, Q. Sol-gel synthesis of $CuO-TiO_2$ catalyst with high dispersion CuO species for selective catalytic oxidation of NO. *Appl. Surf. Sci.* **2017**, *411*, 227–234. [\[CrossRef\]](#)
51. Nestroinaia, O.V.; Ryltsova, I.G.; Lebedeva, O.E. Effect of synthesis method on properties of layered double hydroxides containing Ni(III). *Crystals* **2021**, *11*, 1429. [\[CrossRef\]](#)
52. Wachs, I.E.; Briand, L.E.; Jehng, J.-M.; Burcham, L.; Gao, X. Molecular structure and reactivity of the group V metal oxides. *Catal. Today* **2000**, *57*, 323–330. [\[CrossRef\]](#)
53. Seisenbaeva, G.A.; Cojocaru, B.; Jurca, B.; Tiseanu, C.; Nedelec, J.-M.; Kessler, V.G.; Parvulescu, V.I. Mesoporous tantalum oxide photocatalyst: Structure and activity evaluation. *ChemistrySelect* **2017**, *2*, 421–427. [\[CrossRef\]](#)
54. Liu, M.; Qiu, X.; Hashimoto, K.; Miyauchi, M. Cu(II) nanocluster-grafted, Nb-doped TiO_2 as an efficient visible-light-sensitive photocatalyst based on energy-level matching between surface and bulk states. *J. Mater. Chem. A* **2014**, *2*, 13571–13579. [\[CrossRef\]](#)
55. Wang, D.; Pan, X.; Wang, G.; Yi, Z. Improved propane photooxidation activities upon nano Cu_2O/TiO_2 heterojunction semiconductors at room temperature. *RSC Adv.* **2015**, *5*, 22038–22043. [\[CrossRef\]](#)
56. Li, J.; Zeng, J.; Jia, L.; Fang, W. Investigations on the effect of Cu^{2+}/Cu^{1+} redox couples and oxygen vacancies on photocatalytic activity of treated $LaNi_{1-x}Cu_xO_3$ ($x = 0.1, 0.4, 0.5$). *Int. J. Hydrog. Energy* **2010**, *35*, 12733–12740. [\[CrossRef\]](#)
57. Li, F.; Zhang, L.; Evans, D.G.; Duan, X. Structure and surface chemistry of manganese-doped copper-based mixed metal oxides derived from layered double hydroxides. *Colloids Surf. A Physicochem. Eng. Asp.* **2004**, *244*, 169–177. [\[CrossRef\]](#)
58. Sandulescu, A.; Anastasescu, C.; Papa, F.; Raculete, M.; Vasile, A.; Spataru, T.; Scarisoreanu, M.; Fleaca, C.; Mihailescu, C.N.; Teodorescu, V.S.; et al. Advancements on Basic Working Principles of Photo-Driven Oxidative Degradation of Organic Substrates over Pristine and Noble Metal-Modified TiO_2 . Model Case of Phenol Photo Oxidation. *Catalysts* **2021**, *11*, 487. [\[CrossRef\]](#)
59. Sobczyński, A.; Duczmal, Ł.; Zmudziński, W. Phenol destruction by photocatalysis on TiO_2 : An attempt to solve the reaction mechanism. *J. Molec. Catal. A Chem.* **2004**, *213*, 225–230. [\[CrossRef\]](#)
60. Rydosz, A. The use of copper oxide thin films in gas-sensing applications. *Coatings* **2018**, *8*, 425. [\[CrossRef\]](#)
61. Wu, L.; Bi, J.; Li, Z.; Wang, X.; Fu, X. Rapid preparation of Bi_2WO_6 photocatalyst with nanosheet morphology via microwave-assisted solvothermal synthesis. *Catal. Today* **2008**, *131*, 15–20. [\[CrossRef\]](#)
62. Tang, J.; Zou, Z.; Ye, J. Photocatalytic Decomposition of Organic Contaminants by Bi_2WO_6 Under Visible Light Irradiation. *Catal. Lett.* **2004**, *92*, 53–56. [\[CrossRef\]](#)
63. Yan, H.; Wang, X.; Yao, M.; Yao, X. Band structure design of semiconductors for enhanced photocatalytic activity: The case of TiO_2 . *Prog. Nat. Sci. Mater. Int.* **2013**, *23*, 402–407. [\[CrossRef\]](#)
64. Dey, S.; Ricciardo, R.A.; Cuthbert, H.L.; Woodward, P.M. Metal-to-metal charge transfer in AWO_4 ($A = Mg, Mn, Co, Ni, Cu$, or Zn) compounds with the wolframite structure. *Inorg. Chem.* **2014**, *53*, 4394–4399. [\[CrossRef\]](#)
65. Palasyuk, O.; Palasyuk, A.; Maggard, P.A. Syntheses, optical properties and electronic structures of copper (I) tantalates: $Cu_5Ta_{11}O_{30}$ and $Cu_3Ta_7O_{19}$. *J. Solid State Chem.* **2010**, *183*, 814–822. [\[CrossRef\]](#)

66. Mao, L.; Cai, X.; Gao, H.; Diao, X.; Zhang, J. A newly designed porous oxynitride photoanode with enhanced charge carrier mobility. *Nano Energy* **2017**, *39*, 172–182. [[CrossRef](#)]
67. Jiang, C.-M.; Farmand, M.; Wu, C.H.; Liu, Y.-S.; Guo, J.; Drisdell, W.S.; Cooper, J.K.; Sharp, I.D. Electronic Structure, Optoelectronic Properties, and Photoelectrochemical Characteristics of γ -Cu₃V₂O₈ Thin Films. *Chem. Mater.* **2017**, *29*, 3334–3345. [[CrossRef](#)]
68. Xu, X.; Sun, Y.; Fan, Z.; Zhao, D.; Xiong, S.; Zhang, B.; Zhou, S.; Liu, G. Mechanisms for O₂^{•−} and OH production on flowerlike BiVO₄ photocatalysis based on electron spin resonance. *Front. Chem.* **2018**, *6*, 64. [[CrossRef](#)]
69. Dubale, A.A.; Ahmed, I.N.; Chen, X.-H.; Ding, C.; Hou, G.-H.; Guan, R.-F.; Meng, X.; Yang, X.-L.; Xie, M.-H. A highly stable metal-organic framework derived phosphorus doped carbon/Cu₂O structure for efficient photocatalytic phenol degradation and hydrogen production. *J. Mater. Chem. A* **2019**, *7*, 6062–6079. [[CrossRef](#)]
70. Raciulete, M.; Papa, F.; Kawamoto, D.; Munteanu, C.; Culita, D.C.; Negrila, C.; Atkinson, I.; Bratan, V.; Pandele-Cusu, J.; Balint, I. Particularities of trichloroethylene photocatalytic degradation over crystalline RbLaTa₂O₇ nanowire bundles grown by solid-state synthesis route. *J. Environ. Chem. Eng.* **2019**, *7*, 102789. [[CrossRef](#)]
71. Raciulete, M.; Papa, F.; Negrila, C.; Bratan, V.; Munteanu, C.; Pandele-Cusu, J.; Culita, D.C.; Atkinson, I.; Balint, I. Strategy for Modifying Layered Perovskites toward Efficient Solar Light-Driven Photocatalysts for Removal of Chlorinated Pollutants. *Catalysts* **2020**, *10*, 637. [[CrossRef](#)]
72. Li, T.F.; Liu, J.J.; Jin, X.M.; Wang, F.; Song, Y. Composition-dependent electro-catalytic activities of covalent carbon-LaMnO₃ hybrids as synergistic catalysts for oxygen reduction reaction. *Electrochim. Acta* **2016**, *198*, 115–126. [[CrossRef](#)]